

Review

Mathematical Modeling and Computer Simulations of Nanofluid Flow with Applications to Cooling and Lubrication

Clement Kleinstreuer * and Zelin Xu

Department of Mechanical and Aerospace Engineering, North Carolina State University, Raleigh, NC 27695-7910, USA; zxu4@ncsu.edu

* Correspondence: ck@ncsu.edu; Tel.: +1-919-515-5261

Academic Editors: Phuoc X. Tran and Mehرداد Massoudi

Received: 31 March 2016; Accepted: 20 May 2016; Published: 27 May 2016

Abstract: There is a growing range of applications of nanoparticle-suspension flows with or without heat transfer. Examples include enhanced cooling of microsystems with low volume-fractions of nanoparticles in liquids, improved tribological performance with lubricants seeded with nanoparticles, optimal nanodrug delivery in the pulmonary as well as the vascular systems to combat cancer, and spray-coating using plasma-jets with seeded nanoparticles. In order to implement theories that explain experimental evidence of nanoparticle-fluid dynamics and predict numerically optimum system performance, a description of the basic math modeling and computer simulation aspects is necessary. Thus, in this review article, the focus is on the fundamental understanding of the physics of nanofluid flow and heat transfer with summaries of microchannel-flow applications related to cooling and lubrication.

Keywords: nanofluids; mathematical modeling; computer simulations; heat transfer enhancement; improved lubrication

1. Introduction

Over the last several decades, there has been an ever-increasing interest in nanofluids, *i.e.*, liquids with all sorts of solid nanoparticles (NPs) well dispersed at low concentrations. Application areas for nanofluids range from engineering to medicine, taking advantage of their unique properties in heat transfer [1–3], drug delivery [4–7], mass transport [8,9], boiling phenomena [10,11], absorption and radiation [12–15], optics [16,17], reacting surfaces and catalysts [18], spray-coating [19,20], and lubrication [21–24]. Though initially investigated in the heat transfer community (see [25]), the concept of “nanofluids” is being continuously expanded in developing more and more useful applications. Three application-schematics are given in Figure 1. Clearly, in order to achieve optimal system performance in present and future applications, the underlying physics has to be clearly understood via benchmark experiments as well as sound theories. Focusing here on various aspects of mathematical modeling and computer simulations, transport processes of nanofluids are analyzed and system performances numerically predicted.

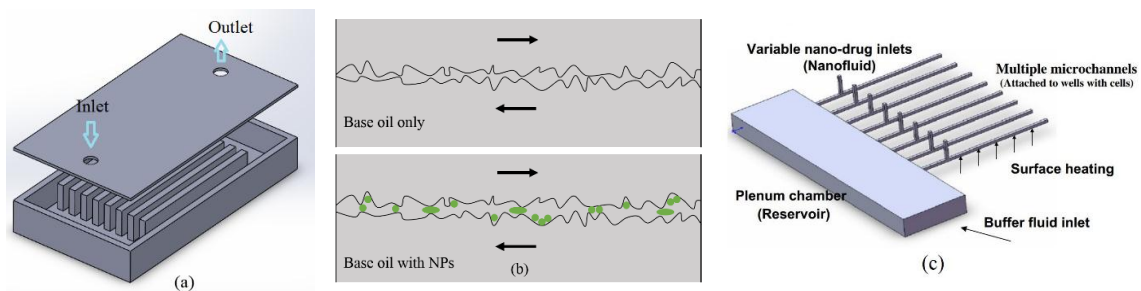


Figure 1. Applications of nanofluids for (a) enhanced microsystem cooling; (b) improved lubrication; and (c) drug delivery [26].

2. Use of Nanofluids in Cooling and Lubrication

2.1. Experimental Evidence

Experimental evidence indicating the advantages of using nanofluids for cooling and lubrication is abundant. In this section, we discuss the measured performance enhancement when using nanofluids in cooling and lubrication in contrast to employing base fluids alone.

2.1.1. Cooling with Nanofluids

One of the main potential applications of nanofluids is enhanced heat transfer, especially the cooling of microsystems with very large heat fluxes. This has been the focus of a number of studies, where microchannel heat sinks (MCHS's) were chosen as heat removal devices. Convection heat transfer in microchannels using conventional fluids such as water and ethylene glycol have been recently reviewed in [27,28]. Nanofluids promise better performance for heat transfer in microchannels than the base liquids, provided that all system components are carefully designed. Largely supportive experimental evidence of improved heat transfer performance when using nanofluids in microsystems is summarized in chronological order as follows.

Chein and Chuang [29] measured the heat transfer and fluid flow characteristics of 0.2–0.4 vol % CuO-water nanofluids in a trapezoidal silicon MCHS. They observed a large enhancement of heat transfer at low flow rates, but little benefit at high flow rates when compared to the base fluid. They attributed this result to the fact that at high flow rates heat is transferred rapidly, whereas nanoparticles (NPs) contribute little to the thermal exchange. While only a slight pressure drop increase was observed in the presence of NPs, nanoparticle deposition was recorded. Jung *et al.* [30] measured the heat transfer and pressure drop of Al₂O₃-water nanofluid flow in rectangular microchannels in the laminar flow regime with NP-volume fractions up to 1.8%. They found that the Nusselt number of the nanofluid flow can be correlated by $Nu = 0.014\phi^{0.095}Re^{0.4}Pr^{0.6}$. The measured increase in convection heat transfer coefficient at 1.8% NP volume fraction was 32% over that of the distilled water, while the measured friction losses were similar for both the nanofluid and the base fluid. Ho *et al.* [31] experimentally assessed the thermal and hydraulic performance of Al₂O₃-water nanofluid flow in a copper MCHS with rectangular microchannels in the laminar flow regime. It was found that the friction factor in the microchannel heat sink cooled by the nanofluid, containing up to 2 vol % NPs, slightly increased relative to the pure water. On the other hand, a 70% increase in average heat transfer coefficient and 25% decrease in MCHS thermal resistance were found by adding 1 vol % NPs to the base fluid at $Re = 1676$. Using nanofluids was found to be more beneficial at higher flow rates. In contrast, the experimental study of Anoop *et al.* [32] showed that, when compared to water, nanofluid heat transfer enhancements occurred at lower flow rates in a microchannel, and heat transfer degradation occurred at higher flow rates due to NP deposition on the microchannel wall. Byrne *et al.* [33] measured the fluid flow and heat transfer characteristics of CuO-water nanofluids in microchannels with NP volume fractions from 0.005% to 0.1%. While a modest improvement in heat transfer was found, the use of a

surfactant was essential in maintaining a proper suspension of NPs in the liquid. Rimbault *et al.* [34] evaluated transitional and turbulent CuO-water flow in a MCHS with NP-diameters of 29 nm and volume fractions ranging from 0.24% to 4.5%. Little heat transfer enhancement was obtained by adding NPs at low concentrations, while a clear decrease was found at high concentrations. On the other hand, a large pressure drop increase (up to 70% at 4.5 vol %) with respect to water was found for all NP-loading ranges. This is the only study presenting results of transitional and turbulent nanofluid flow in microsystems, which is opposite to the beneficial findings for thermal nanofluid flow in the laminar regime. Indeed, the observed deterioration in heat transfer was confirmed by the authors of [35], who analyzed Al₂O₃-water flow in a mini-channel. Rimbault *et al.* [34] suggested that particle migration towards the wall and enhanced local particle deposition may be the reasons. Manay and Sahin [36] experimentally determined the effect of the aspect ratio of microchannels on nanofluid heat transfer. While nanofluids provided better heat transfer performance without causing excessive pressure drop, reduced heat transfer and increased pressure drop were generated by nanofluid flow in microchannels with high aspect ratios. Azizi *et al.* [37] studied the thermal performance and friction factor of a cylindrical MCHS cooled by Cu-water nanofluids. The results showed that the presence of NPs enhanced the entrance Nusselt number up to 43%; however, the friction factor also increased up to 45.5% when compared to the base fluid.

Some of the experimental evidence of the heat transfer performance of nanofluids in microsystems is shown in Figures 2–4. It can be seen that, based on available data, nanofluids significantly enhance the heat transfer performance in microsystems as compared with that of the base fluids at elevated Reynolds numbers, *i.e.*, $Re > 100$. Yet in the low Re -number region, both enhanced and reduced heat transfer were measured. Severe fouling in microchannels was suggested to be the reason for heat transfer deterioration. Little data exist for turbulent nanofluid flow in microsystems. Concerning friction characteristics of nanofluid flow in microsystems, the data are more scattered. Most of the studies concluded that a minor pressure drop increase was detected when adding NPs to the base fluid. However, Chevalier *et al.* [38] measured the rheological properties of nanofluids flowing through microchannels and obtained much higher effective viscosities than those predicted by the Einstein equation (see Equation (26) in Section 3). This suggests that the thermal performance of nanofluids may be compromised.

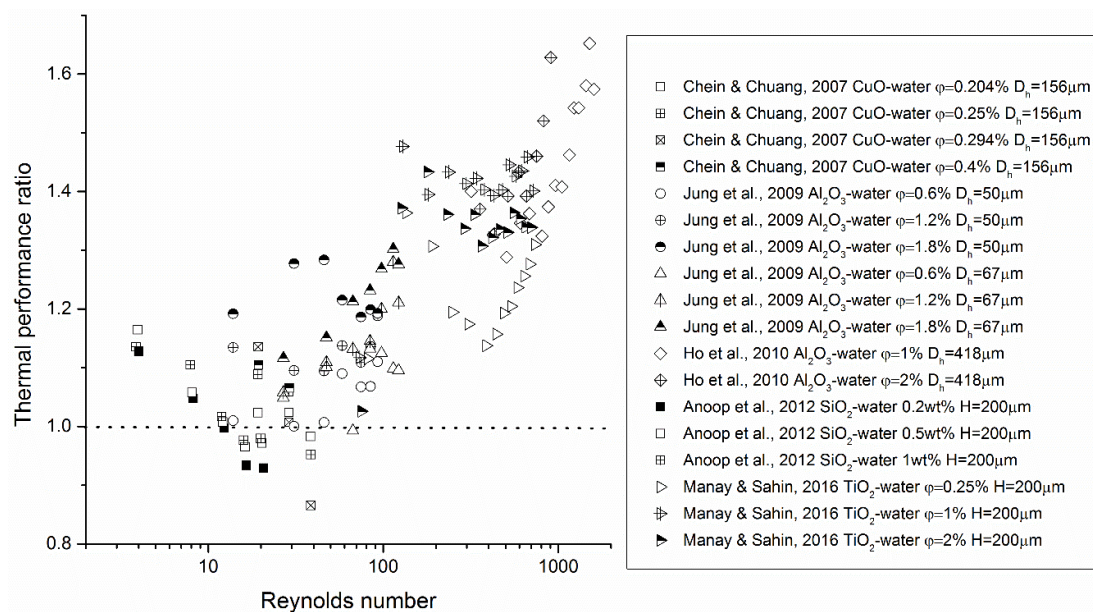


Figure 2. Experimental evidence of thermal performance of nanofluid flow in microsystems. The thermal performance ratio in this figure represents h_{nf}/h_{bf} or $(1 - R_{nf}/R_{bf}) + 1$ depending on how the data were originally presented in the references, where R is the heat sink thermal resistance.

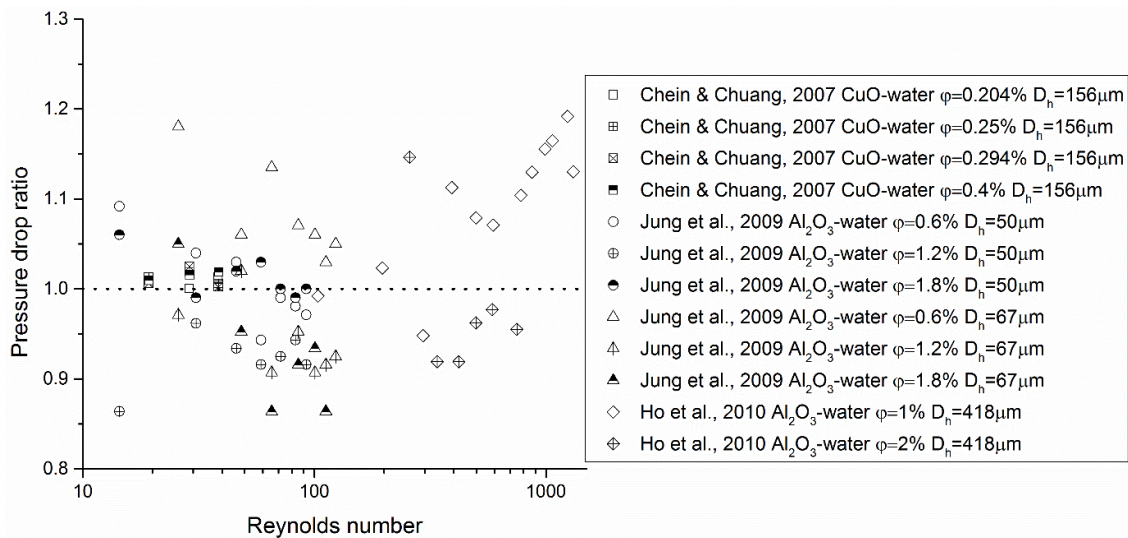


Figure 3. Experimental evidence of hydraulic characteristics of nanofluid flow in microsystems. The pressure drop ratio in this figure represents $\Delta p_{nf}/\Delta p_{bf}$ or f_{nf}/f_{bf} depending on how the data were originally presented in the references, where f is the friction factor.

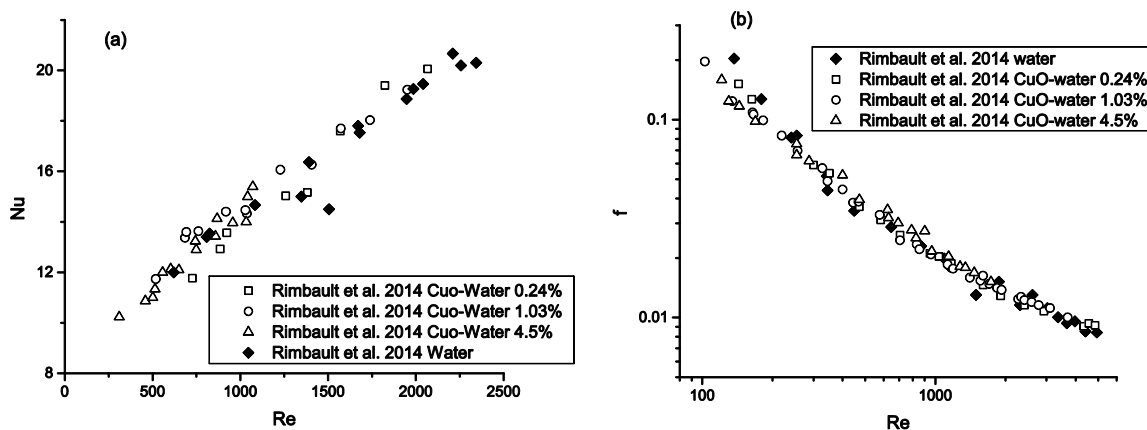


Figure 4. Thermal (a) and hydraulic (b) performance of nanofluid flow in a MCHS in laminar, transitional, and turbulent regime. The dashed line is used as a guide [34].

2.1.2. Nanoparticles in Lubrication

Friction is one of the main causes of energy loss in mechanical systems. In fact, machine elements usually fail due to excessive wear. Hence, it is essential to provide superior lubrication to improve the efficiency of energy utilization and the reliability of mechanical systems. Adding nanoparticles to the lubricants can enhance their tribological properties, especially in the boundary and mixed lubrication regimes. The anti-friction and anti-wear behaviors of a variety of nanoparticles used as lubricant additives have been reported [39], including metals (e.g., Zn, Cu, Ni, Fe, Co, Pd, and Au), metal oxides (e.g., TiO_2 , Al_2O_3 , CuO, ZnO, ZrO_2 , and $ZnAl_2O_4$) and their composites, sulfides (e.g., WS_2 , MoS_2 , CuS, and ZnS), nonmetals (e.g., diamond, SiO_2 , carbon nanotubes, and fullerenes), inorganic oxythiomolybdates (e.g., $Cs_2MoO_2S_2$, $ZnMoO_2S_2$), and boron-based nanoparticles (e.g., calcium borate, zinc borate, boron nitride, and alkali borates). Most of the evidence indicates that adding NPs to the lubricants can significantly improve lubrication performance by reducing both friction and wear, thereby allowing for an increase in load-carrying capacity [21,40–51]. A number of mechanisms have been proposed to explain the superior performance of lubricants with nanoparticle additives, including surface adsorption, penetration into asperities, and tribo-chemical reaction to reduce wear, as well

as size effect, colloidal effect, exfoliation, protective film, and third-body effect to reduce friction (see Figures 5 and 6).

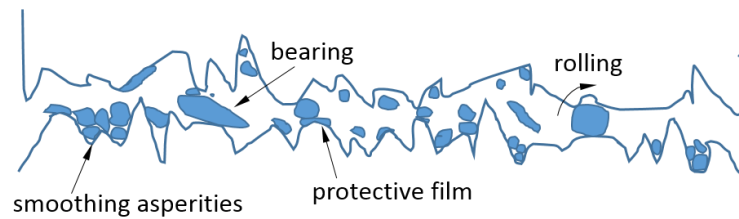


Figure 5. Scheme of third body under friction with nanoparticles.

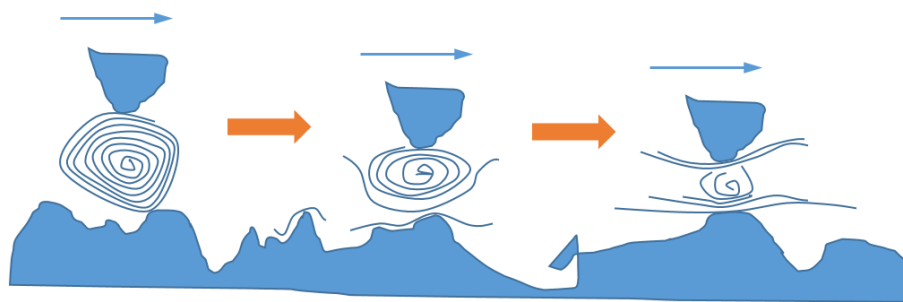


Figure 6. Schematic presentation of the exfoliation process: individual nanotube exfoliation. Exfoliation can also happen on nano-sheets from aggregates, from smearing the nanotubes, and by breaking large NPs into smaller pieces (see [52]). The arrows indicate the sliding direction.

The focus of this review is on the enhanced lubrication performance when using nanoparticles and the underlying mechanisms. The different factors that affect the tribological properties as well as different applications are discussed.

Early attempts in using small particles to enhance lubricants were made decades ago. For example, Bartz [53] investigated the influence of the particle-diameter range of 0.7–7 μm on the lubricating effectiveness of MoS_2 -suspensions using a four-ball tester. The author found that finer particles only improved wear performance at high loads with smooth surfaces. He suggested that temperature, material, and surface roughness must be taken into account in order to transfer these results to conditions different from the four-ball tester. Cusano and Sliney [54,55] added sub-micron graphite and MoS_2 particles to a mineral oil and found deleterious effects under boundary lubrication conditions of a Hertzian contact.

Tao *et al.* [21] added 1% diamond nanoparticles with a 5-nm average diameter to paraffin oil. The results indicated that, under boundary-lubrication conditions, the nanofluid lubricant exhibited excellent load-carrying capacity, anti-wear, and friction-reduction properties. The authors postulated that the nanoparticles lodge into the rubbing surfaces due to their small size and in effect polish the surface. At the same time, some nanoparticles may form an inlaid pattern into the surface, which raises the hardness of the rubbing surface. Under extended rubbing time, the nanofluid forms a boundary lubricating film between the gliding surfaces. The NPs in the film not only bear the loading but also separate the solid parts and hence prevent their direct contact. They can also roll between the polished surfaces. This ball-bearing effect of nanoparticles also increases the load-bearing capacity while reducing wear and friction.

Subsequent studies [40–43] confirmed that adding nanoparticles to paraffin and water at low concentrations greatly improved the load-carrying capacity as well as the anti-wear and friction-reduction properties. A boundary protective film, consisting of nanoparticles, was found to form between the gliding surfaces [56,57]. Qiu *et al.* [58] suggested that the forming of a third body due to the deposition of nanoparticles on the contacting surfaces led to the observed lubrication

behavior, which was supported in [44,45]. Some studies supported the mending effect, *i.e.*, the healing of the surface during the tribological test, which may be due to exfoliation of NPs [46]. Nanoparticles fill the dimples and somewhat smooth the asperities, with a tribo-chemical reaction on the friction surfaces [47–49,59]. This is similar to the surface polishing effect proposed in [21]. Mosleh *et al.* [60] suggested two mechanisms of reducing asperity contact using nanoparticles: (1) filling the micro-valleys of contacting surfaces [51]; and (2) shearing NPs at the interface [61].

The mechanisms may be different, however, if nanoparticles with high aspect ratios or special material structures are used, e.g., inorganic nanotubes and fullerene-like nanoparticles [46,62]. In such cases, exfoliation of the platelet-shaped NPs may play a more significant role in friction and wear reduction [51,52,63–65]. Figure 6 illustrates the mechanism of friction and wear reduction due to NP exfoliation. Specifically, NPs exfoliate under load and form an adherent film of thin flakes on the surfaces in contact. At high pressure, when greases or oils are squeezed out, this film can still act as a lubricant [66,67].

The lubrication effectiveness of the nanofluid matrix is strongly affected by a number of factors, including the physical and chemical properties of the nanoparticles, particle size, temperature in the contact region, particle concentration, particle aggregation, the presence of extreme pressure agents, type of base fluid, and the test conditions. The effects of some of these factors on lubrication properties are shown in Figures 7–9. Finer particles tend to provide better tribological properties, while an optimal particle concentration seems to exist for each NP-lubricant pair. At elevated temperatures, the viscosity of the base fluid is greatly reduced, leading to direct contact of the nanoparticles with the sliding surfaces, hence improving the lubrication effectiveness. Mechanically hard materials exhibit better load-carrying capacities and friction-reducing properties, due to their higher yield strength. However, they may lead to more surface wear. Nanofluid lubricants may be more effective in the boundary-lubrication regime, due to the high contact pressure that drains the fluids. In elasto-hydrodynamic lubrication and film-lubrication regimes, the liquid film plays a more important role [68–70].

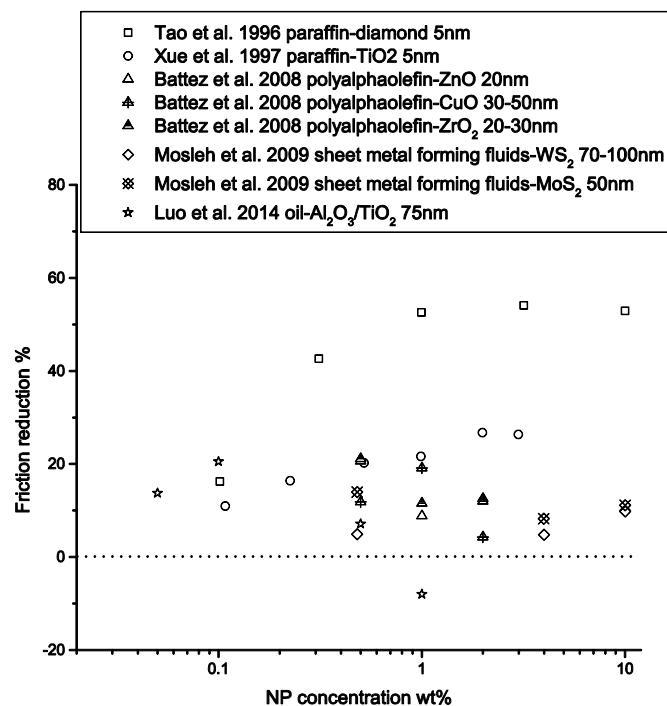


Figure 7. Performance of nanoparticle-enhanced lubricants in friction reduction as a function of NP concentration. The friction reduction is calculated as $1 - f_{nf}/f_{bf}$, where f is the friction coefficient.

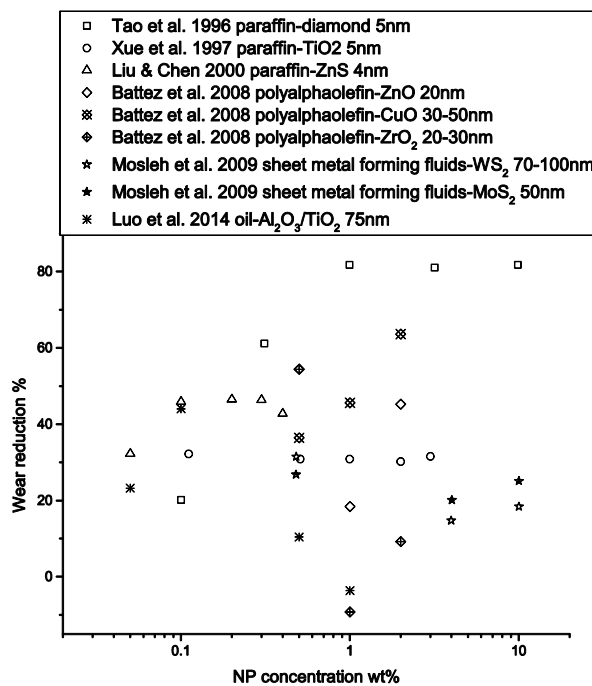


Figure 8. Performance of nanoparticle-enhanced lubricants in wear reduction as a function of NP concentration. The wear reduction is calculated as $1 - \varepsilon_{nf}/\varepsilon_{bf}$, where ε represents wear scar diameter, wear volume, or wear rate, depending on the form of the data provided in the original studies.

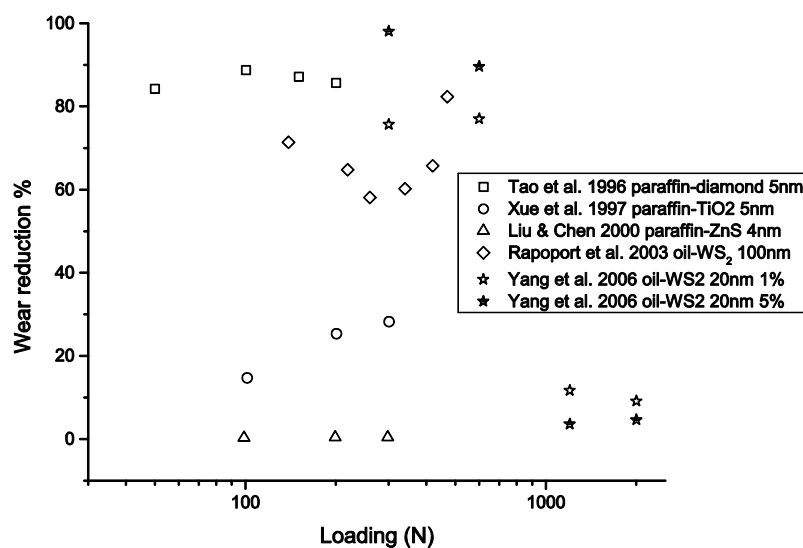


Figure 9. Performance of nanoparticle-enhanced lubricants in improved load-carrying capacity as a function of loading. The wear reduction is calculated as $1 - \varepsilon_{nf}/\varepsilon_{bf}$, where ε represents wear scar diameter, wear volume, or wear rate, depending on the form of the data provided in the original studies.

The effective use of nanofluid lubricants have been also examined for other applications. For example, the lubrication performance of nanofluids for minimal quantity lubrication (MQL) in grinding processes was evaluated [71–74]. It was shown that nanoparticle-jet MQL achieved cooling and lubrication effects close to that of flood lubrication. Hybrid nanoparticles have better lubrication effects caused by the “physical synergistic effect,” which integrates the lubrication advantages of different NPs for better overall performance. Yu *et al.* [75,76] studied the role of the oxide-scale on the tribological behavior in the nanoparticle lubrication of hot rolling. Again, nanoparticles were found to

be trapped in the cracks, which changed the wear rates. Zareh-Desari *et al.* [77] studied the effect of NP additives on lubrication performance in a deep drawing process and found that adding NPs to the base lubricant reduces the required forming load and improved the surface quality of the formed cups.

Stability of nanofluids is critical to their consistent performance in enhancing the tribological properties of the lubricants. A typical method to stabilize the nanofluid is to modify the NP surface [78–81]. To deal with the adverse effect of nanoparticle aggregation on the lubrication properties, Verma *et al.* [82] designed a low-cost approach to allow the intercalation of MoS₂ nanoparticles with organic agents, activating the inorganic nanoparticles. They proposed that the nanoparticles could bond to specific active agents and act as nano-reservoirs to store these additives. Once the NPs steer through the asperities of the contacting surfaces, they can deliver the organic agents and thus achieve specific functions. This idea is in the same vein as the methodology of targeted nanodrug delivery [5]. Recent experimental studies, focusing on reduced friction, anti-wear, and enhanced load-carrying capacity, have explored different NP materials and various surfactants to stabilize the mixture [52,70,83–90].

2.2. Theoretical Background

The laboratory examples presented in Section 2.1 indicate that the use of nanoparticles in coolants and lubricants can be quite advantages, *i.e.*, leading to improved efficiency and reliability, respectively. In this section, the underlying physics in terms of forces acting on nanoparticles as well as nanofluid properties are discussed in preparation for the subsequent sections on math modeling and computer simulations [91].

2.2.1. Forces Acting on Nanoparticles

In nanofluids, Brownian agitation of nanoparticles typically overcomes particle-sedimentation, resulting in mixture properties that are determined by both the nanoparticles and the base fluid. The very large surface-to-volume ratio and the very small inter-particle distance endow nanofluids with many unique properties. Fundamental are the forces experienced by each nanoparticle in the base fluid. Here, we give a brief discussion of the various NP-displacement velocities due to forces acting on the nanoparticles, explaining the microscopic mechanisms that give rise to the unique properties of nanofluids.

Random force. The random force $\vec{F}_B(t)$ that derives from the collisions between particles and the randomly moving molecules of the base fluid gives rise to the Brownian motion of the nanoparticles. Based on the Langevin equation and the equilibrium-partition theorem, the stochastic process causes an average instantaneous nanoparticle velocity of \vec{v}_p , which can be expressed as

$$\vec{v}^{BM} = \sqrt{\frac{3\kappa_B T}{m_p}}, \tag{1}$$

where $\kappa_B = 1.38 \times 10^{-23} \text{ m}^2 \cdot \text{kg} \cdot \text{s}^{-2} \cdot \text{K}^{-1}$ is the Boltzmann constant, T is the local temperature, and \vec{v}^{BM} is the Brownian motion velocity of a typical nanoparticle with mass m_p in a time scale of $t \ll \tau$, where τ is the particle momentum relaxation time. The collective effect of the random motion of nanoparticles is the dispersion of particles, which can be expressed by a dispersion coefficient, D_0 :

$$D_0 = \frac{k_B T}{3\pi\mu_b d_p}, \tag{2}$$

where d_p is the particle diameter. The effects of the Brownian motion can be incorporated by a random force, \vec{F}_{Br} , whose effect is to cause a dispersion equivalent to that predicted by Equation (3):

$$\vec{F}_{Br} = \frac{m_p}{\pi} \vec{R} \sqrt{\frac{2k_B T}{3\pi\mu d_p (\Delta t)^3}}, \quad (3)$$

where \vec{R} is a random vector whose components are Gaussian random numbers with zero mean and unit variance, and Δt is the integration time which is much higher than the characteristic time of molecular collisions.

Thermophoretic force. Particles can diffuse under the effect of a temperature gradient, where particles migrate from hotter to colder regions and cause a higher concentration of nanoparticles in the colder regions. This phenomenon is called thermophoresis and is equivalent to the Soret effect for gaseous or liquid mixtures. The thermophoresis effect can be expressed in terms of a thermophoretic velocity:

$$\vec{v}_{tp} = -K_{tp} \frac{\mu_f}{\rho_f} \frac{\nabla T}{T}, \quad (4)$$

or, equivalently, a thermophoretic force

$$F_{tp} = -3\pi\mu^2 d_p K_{tp} \frac{\nabla T}{\rho_f T_\infty}, \quad (5)$$

where the proportionality factor K_{tp} is a function of the thermal conductivities of both the fluid and the solid particles. The expression of K_{tp} for aerosols is given as

$$K_{tp} = \frac{2C_s(k_{bf} + 2k_p Kn)}{(1 + 6C_m Kn)(2k_{bf} + k_p + 4k_{bf} C_t Kn)}, \quad (6)$$

where the parameters C_s , C_m , and C_t can be determined empirically with numerical values of 1.17, 1.14, and 2.18, respectively, for $Kn < 0.1$ [92]. Here, $Kn = \ell/d_p$ is the Knudsen number, and ℓ is the mean free path of molecules. For thermophoresis of relatively large particles (1 μm) in liquids, the following expression can be used [93]:

$$K_{tp} = 0.26 \frac{k_{bf}}{2k_{bf} + k_p}. \quad (7)$$

It should be noted that thermophoresis is a direct consequence of the Brownian motion of particles. It has the same cause as the Brownian diffusion of particles as discussed above.

Body force. Nanoparticles may experience different field forces depending on the types of applications. Typically, the gravitational force applies due to the density difference between the nanoparticles and the base fluids:

$$F_g = \frac{1}{6} \pi d_p^3 \Delta\rho, \quad (8)$$

which gives rise to a settling velocity,

$$v_s = \frac{\Delta\rho g d_p^2}{18\mu_{bf}}, \quad (9)$$

where μ_{bf} is the base fluid viscosity, $\Delta\rho$ is the density difference between the nanoparticle and the base fluid, d_p is the particle diameter, and g is the gravitational constant.

In an applied electrical field, particles will undergo electrophoretic motion with a velocity of v_{el} , i.e.,

$$v_{el} = \frac{\sigma d_p E}{3\mu_{bf}}, \quad (10)$$

where σ is the surface charge density of the particle, and E is the applied electric field. This force is due to an externally applied field. Forces due to the charges of NPs will be discussed later.

Stokes force. When a nanoparticle moves relative to the base fluid, it experiences a drag force. At particle Reynolds numbers of $Re \leq 1$, the drag force can be expressed according to Stokes' law as

$$\vec{F}_{Stokes} = 3\pi\mu_{bf}d_p\vec{v}'_p \tag{11}$$

where \vec{v}'_p is the instantaneous particle velocity relative to the base-fluid motion.

An important parameter in the analysis of particle motion in a fluid is the relaxation time defined as

$$\tau_p = \frac{m_p\vec{v}'_p}{\vec{F}_{Stokes}} = \frac{m_p}{3\pi\mu_{bf}d_p} \tag{12}$$

This characterizes the time required for a particle to adjust to or relax its velocity to a new condition of forces.

Inter-particle forces. When two particles approach each other due to Brownian motion, the attractive van der Waals forces and the repulsive electrostatic force become important.

The van der Waals forces cause attraction between particles. The attraction potential is proportional to the particle diameter, the material constant (the Hamaker constant A_H), and is inversely proportional to the distance of separation:

$$\psi_{LD} = -\frac{A_H}{12} \left[\frac{1}{x(x+2)} + \frac{1}{(x+1)^2} + 2\ln\frac{x(x+2)}{(x+1)^2} \right], \tag{13}$$

where $x = h/d_p$. For small particle separations ($h \ll d_p$), Equation (13) is reduced to

$$\psi_{LD} = -\frac{A_H d_p}{24h} \tag{14}$$

The average (minimum) separation distance between two spheres in a well-dispersed suspension can be obtained via

$$h = \frac{d_p}{2} \left[\left(\frac{0.64}{\varphi} \right)^{\frac{1}{3}} - 1 \right], \tag{15}$$

where φ is the nanoparticle volume fraction. According to Equation (15), the average particle distance scales with the particle diameter and hence becomes very small for nanoparticles.

When two particles approach each other, the ionic atmospheres overlap and create an ion concentration difference between the overlapped region and the bulk. This difference gives rise to an osmotic pressure acting to force the particles apart. The potential of this repulsive force can be obtained by integrating the force over distance [94]:

$$\psi_{EDL} = 32\pi d_p \kappa_B T \kappa^{-2} \rho_{el} \tanh^2 \left(\frac{\sigma e \phi_0}{4\kappa_B T} \right) \exp(-\kappa h), \tag{16}$$

where κ_B is the Boltzmann constant, σ is the valence of the ions, κ is the Debye constant which is the inverse of the Debye length, ρ_{el} is the concentration of electrons, e is the electronic charge, and ϕ_0 is the electric double layer (EDL) potential at the surface of the nanoparticles. The expression is valid when the value of the product, κd_p , is greater than 20, and becomes invalid when the double-layer thickness is about the same as or larger than the particle radius. For the latter situation, the potential equations for the interaction between two double layers must be solved specifically for spherical particles. This is especially important for nanofluids because, for metal-oxide nanofluids and metal nanofluids, κd_p is usually less than 4 [95].

Relative importance of these forces. An order-of-magnitude analysis of the Stokes force and the inter-particle forces in nanofluids has been provided in [96]. In dilute nanofluids, the surface forces, *i.e.*, the van der Waals forces and the electrostatic force, are of the same order as the Stokes force if multi-particle interactions are considered. Meanwhile, Buongiorno [97] has shown that body forces are negligible compared to the random force that causes Brownian diffusion. However, the surface forces are only important when nanoparticles are well dispersed in the base fluid. When nanoparticle aggregation occurs, the surface forces become less important, while wake interactions due to Brownian motion dominate.

2.2.2. Nanoparticle Aggregation

Nanoparticle aggregation is one of the most important factors that may affect any consistent performance of the majority of nanofluids [98,99]. Due to the large surface area of NPs and the small average particle distance, NPs are prone to aggregation due to the inter-particle forces. Aside from potentially enhancing the effective thermal conductivity of a nanofluid, NP-aggregation may also lead to heterogeneous mixture properties and particle settling. However, it is very difficult to qualify, let alone quantify, the aggregation process due to the inevitable heterogeneous nature of nanofluids. It is a phenomenon caused by the inter-particle forces; however, it cannot be categorized as a nanofluid property. Statistical methods can be used only to a certain extent because of the high dependence on NP-material type and the NP-preparation method. One way to quantify NP-aggregation is to use the method developed by Nan *et al.* [100] for colloidal systems, as has been adopted in [14] among others. NP-aggregation affects nearly every property of the nanofluids by modifying the micro-structures of the mixture. It can be mediated by adding surfactants to the nanofluids or by altering the pH value of the mixture, both of which enhance the stability of nanoparticles in aqueous suspensions by introducing repulsive forces between NPs.

2.2.3. Thermo-Physical Properties of Nanofluids

Considering the forces experienced by NPs provides a microscopic view that serves as the basis for the discussion of macroscopic properties exhibited by nanofluids. In this section, we discuss the bulk properties of nanofluids and their mathematical description, which can then be used in the governing equations to predict nanofluid performances for various applications.

The basic particle-fluid mixture properties are greatly a function of the particle volume fraction. If particles are assumed to be spherical, mono-disperse, and forming a homogeneous dilute suspension, the nanofluid density and heat capacity in the case of low NP-volume fractions can be expressed as

$$\rho_{nf} = \varphi \rho_p + (1 - \varphi) \rho_{bf}, \tag{17}$$

and

$$(\rho c_p)_{nf} = \varphi (\rho c_p)_p + (1 - \varphi) (\rho c_p)_{bf}, \tag{18}$$

where the subscripts *bf*, *p* indicate base fluid and particle, respectively.

Thermal conductivity of nanofluids. Certain nanofluids have shown significantly enhanced thermal conductivities over their base fluids. It has been shown that the effective thermal conductivity of the mixture k_{nf} increases with the nanoparticle volume fraction and temperature, and with the decrease of particle size (see Figure 5). In addition, particle shape, pH, and aggregation also have significant effects on k_{nf} .

Assuming a monodisperse suspension spherical particles, Maxwell [101] derived the effective thermal conductivity of fluid-particle mixture as

$$k_{eff} = k_{bf} \cdot \left(1 + \frac{3 \left(\frac{k_p}{k_{bf}} - 1 \right) \varphi}{\left(\frac{k_p}{k_{bf}} + 2 \right) - \left(\frac{k_p}{k_{bf}} - 1 \right) \varphi} \right), \tag{19}$$

where k_{bf} and k_p are the thermal conductivities of the base fluid and the nanoparticle material, respectively. This model predicts the k_{eff} of mixtures with particle sizes greater than 1 μm . However, it significantly underestimates the effective thermal conductivity of nanofluids.

Brownian motion and particle aggregation are arguably the most fundamental effects that characterize nanofluids. The Brownian motion of nanoparticles results in micro-scale mixing effects and causes an enhanced effective thermal conductivity, while locally small cluster-like structures due to aggregation can form thermal pathways and augment heat transfer, resulting in enhanced k_{nf} -values.

For example, Kleinstreuer and Feng [96] proposed a model based on Brownian motion-induced micro-convection. Xu and Kleinstreuer [15] enhanced the F-K model to include the local clustering effect as well as the interfacial thermal resistance effect. The model divides the thermal conductivity k_{nf} of the nanofluid into a static part and a micro-mixing part, i.e., $k_{nf} = k_{static} + k_{mm}$. In this equation, k_{static} is similar to Maxwell's model, except that the nanoparticle thermal conductivity k_p in the original Maxwell model is replaced by the effective thermal conductivity of particle aggregate unit k_a :

$$k_a = k_{de} \cdot \frac{3 + \varphi_b [2\beta_{11} (1 - L_{11}) + \beta_{33} (1 - L_{33})]}{3 - \varphi_b (2\beta_{11} L_{11} + \beta_{33} L_{33})}, \tag{20}$$

while

$$k_{mm} = 19631 \cdot C_c \varphi \frac{k_B \tau_a}{m_a} (\rho c_p)_{nf} (\bar{T} \cdot \ln \bar{T} - \bar{T}). \tag{21}$$

Here,

$$k_{de} = (3\varphi_{de} - 1)k_{peff} + (2 - 3\varphi_{de})k_{bf} + \sqrt{[(3\varphi_{de} - 1)k_{peff}]^2 + [(2 - 3\varphi_{de})k_{bf}]^2 + 2[2 + 9\varphi_{de}(1 - \varphi_{de})]k_{peff}k_{bf}}. \tag{22}$$

The effective thermal conductivity of the nanoparticles including the thermal contact resistance, k_{peff} , is given as

$$k_{peff} = \frac{k_p}{1 + R_K k_p / d_p}. \tag{23}$$

In these equations, k_{de} is the effective thermal conductivity of the mixture of base fluid and dead-end particles, φ_{de} is the volume fraction of dead-end particles in an aggregate unit, φ_b is the volume fraction of backbone particles in an aggregate unit, and L_{ii} and β_{ii} are parameters appearing in the derivation of the effective thermal conductivity of arbitrary isotropic particulate composites with interfacial thermal resistance. For a detailed explanation of these parameters, see Section 2.5 of Xu [91]. In addition, R_K is the Kapitza resistance, ρ is the density, c_p is the specific heat capacity, and \bar{T} is the time-averaged temperature. The subscripts p and a denote nanoparticle and aggregate unit, respectively. C_c (≈ 1) is a correction factor that depends on nanoparticle-based fluid pairings. For example, $C_c = 1.1$ for Al_2O_3 -water nanofluids. The characteristic time interval τ_a is expressed as

$$\tau_a = \frac{m_a}{3\pi\mu_{bf}R_g}, \tag{24}$$

where R_g is the average radius of the aggregate units:

$$R_g = 2.5d_p \sqrt{\frac{\varphi}{0.01}} \cdot \sqrt{\frac{T_0}{\bar{T}}}. \tag{25}$$

Here, d_p is the nanoparticle diameter, and $T_0 = 273$ K is the reference temperature.

Comparison with measurements indicated that this model is applicable for several types of metal oxide nanoparticles in water for the range of volume fractions up to 10% and mixture temperatures below 350 K.

A few different mechanisms have been proposed to explain the anomalous enhancement of the mixture thermal conductivity. For example, the base-fluid molecules form layered structures at the particle surface, acting as thermal bridge between the liquid and the solid particles, and thus enhance the k_{nf} [102]. However, there are strong debates about whether they are really important to the enhanced thermal conductivity.

Viscosity of nanofluids. Measurements of the rheological properties of nanofluids indicate that most nanofluids behave as Newtonian-fluid mixtures at low particle volume concentrations [103,104]. Particle concentration, size [105], shape [106], temperature, shear rate [107], surfactants, and pH have direct impacts on the viscosity of nanofluids. For example, viscosity increases with higher particle volume fractions, while it decreases with elevated temperatures. However, due to the aggregation effect of nanoparticles, it is difficult to determine how the particle size affects the effective viscosity. Surfactants and pH affect μ_{nf} mainly by enhancing the dispersion of nanoparticles.

Einstein [108] developed a formula for the effective viscosity of fluids containing spherical particles at low volume fractions (<2%). It indicates a linear increase in viscosity with particle volume fraction:

$$\frac{\mu_{eff}}{\mu_{bf}} = 1 + 2.5\varphi, \tag{26}$$

where μ_{eff} and μ_{bf} are the viscosities of the mixture and the base fluid, respectively. Brinkman [109] extended this model to consider moderate particle concentrations up to 4%:

$$\frac{\mu_{eff}}{\mu_{bf}} = (1 - \varphi)^{2.5}. \tag{27}$$

Comparison with experimentally measured data indicated that the Einstein model and the Brinkman model tend to underestimate the viscosity of nanofluids. In addition, these two models only account for the effect of particle loading on the mixture viscosity but neglect other important influencing factors such as temperature, particle size, and pH. In addition, newly proposed theoretical formulas are not able to accurately predict the effective viscosity for a wide range of nanofluids [104]. Since theoretical models for the viscosity of the mixture usually rely on the homogeneous-dispersion assumption, it is perhaps impossible to derive a general correlation that is able to accurately predict μ_{nf} , given that the aggregation of nanoparticles almost always lead to a heterogeneous mixture. Still, due to the substantial difference among the available experimental data of μ_{nf} , specific empirical correlations that are applicable to only one or a few types of nanofluids and within specific ranges of the pertinent parameters seem to be a more acceptable option at this moment. For example, Corcione [110] obtained an empirical correlation for μ_{nf} with nanoparticles ranging in diameter from 25 nm to 200 nm, volume fractions ranging from 0.01% to 7.1%, and temperatures ranging from 293 to 333 K. The correlation reads

$$\mu_{nf} = \frac{\mu_{bf}}{1 - 34.87 \left(d_p/d_{bf} \right)^{-0.3} \varphi^{1.03}}, \tag{28}$$

where d_{bf} is the equivalent diameter of a base fluid molecule, given by

$$d_{bf} = \left(\frac{6M}{N\pi\rho_{bf0}} \right)^{1/3}, \tag{29}$$

in which M is the molecular weight of the base fluid, N is the Avogadro number, and ρ_{bf0} is the mass density of the base fluid calculated at temperature $T_0 = 293$ K.

Convection heat transfer coefficient. Convection heat transfer performance is the most important measure of thermal nanofluid flow. Heat transfer performance for Fourier-type processes is characterized by the convective heat transfer coefficient or the Nusselt number, *i.e.*,

$$h = \frac{q_w}{T_w - T_f}, \quad (30)$$

while

$$\text{Nu}_x = \frac{h \cdot x}{k}, \quad (31)$$

where q_w is the local wall heat flux, and Nu_x is the Nusselt number at location x .

The Nusselt number excludes the effect of increased pumping cost due to the dispersion of nanoparticles in the base fluid. Hence, the thermal performance factor may be used to evaluate the performance of thermal nanofluid flow:

$$\eta = \frac{\text{Nu}_{nf}/\text{Nu}_{bf}}{\left(f_{nf}/f_{bf}\right)^{1/3}}. \quad (32)$$

When corresponding nanofluid properties are used, the friction factor correlations developed for pure fluids may still be valid for nanofluids in both laminar and turbulent flow regimes. However, it is under debate whether the conventional correlations for the Nusselt number can remain accurate in predicting the nanofluid heat transfer characteristics [111,112]. While experimentally determined Nu of laminar nanofluid flow scatters, the Dittus-Boelter equation can still predict quite accurately the enhancement turbulent heat transfer coefficient of nanofluids [113], *i.e.*,

$$\text{Nu} = 0.023 \text{Re}^{4/5} \text{Pr}^n, \quad (33)$$

where $n = 0.4$ for heating (wall hotter than the bulk fluid), and $n = 0.33$ for cooling. Again, in Equation (33), nanofluid properties should be used in calculating Re and Pr .

2.3. Transport Equations and Modeling Approaches

The dominant forces that determine the nanofluid properties have been given in Section 2.1, while the bulk properties of nanofluids have been discussed in Section 2.2. In this section, the transport equations and modeling approaches for nanofluids are discussed. While there are a number of numerical techniques that can be used to simulate nanofluid flow, the underlying governing equations are all based on force balances and conservation laws. Focusing here on basic engineering applications, numerical techniques that could provide high-fidelity results and probe into the microscopic phenomena through extensive computations may be found elsewhere [114–117].

2.3.1. Single-Phase Approach

In the single-phase approach, the suspended nanoparticles are assumed to be in thermal equilibrium with the liquid phase, and the relative velocity between the two phases can be neglected. The reasoning is that nanoparticles are so small, say, $d_p < 100$ nm, that they closely follow the fluid streamlines, causing the nanofluid to behave like a homogeneous mixture [103]. Thus, the single-phase Navier-Stokes equations can be used with the effective thermo-physical properties of nanofluids, as follows:

Continuity equation:

$$\frac{\partial \rho_{nf}}{\partial t} + \frac{\partial}{\partial x_i} (\rho_{nf} u_i) = 0; \quad (34)$$

Momentum equation:

(Laminar flow)

$$\frac{\partial(\rho_{nf}u_i)}{\partial t} + \frac{\partial}{\partial x_j}(\rho_{nf}u_i u_j) = -\frac{\partial p}{\partial x_i} + \frac{\partial}{\partial x_j} \left[\mu_{nf} \left(\frac{\partial u_i}{\partial x_j} + \frac{\partial u_j}{\partial x_i} \right) \right], \text{ and} \quad (35)$$

(Turbulent flow)

$$\frac{\partial(\rho_{nf}u_i)}{\partial t} + \frac{\partial}{\partial x_j}(\rho_{nf}u_i u_j) = -\frac{\partial p}{\partial x_i} + \frac{\partial}{\partial x_j} \left[\mu_{nf} \left(\frac{\partial u_i}{\partial x_j} + \frac{\partial u_j}{\partial x_i} \right) - \rho_{nf} \overline{u_i u_j} \right]; \quad (36)$$

Energy equation:

(Laminar flow)

$$\frac{\partial(\rho_{nf}h)}{\partial t} + \frac{\partial}{\partial x_i} \left[(\rho c_p)_{nf} u_i T \right] = \frac{\partial}{\partial x_i} \left(k_{nf} \frac{\partial T}{\partial x_i} \right) + \mu_{nf} \Phi, \text{ and} \quad (37)$$

(Turbulent flow)

$$\frac{\partial(\rho_{nf}h)}{\partial t} + \frac{\partial}{\partial x_i} (\rho_{nf}u_i h_{tot}) = \frac{\partial}{\partial x_i} \left(k_{nf} \frac{\partial T}{\partial x_i} - \rho_{nf} \overline{u_i h} \right) + \mu_{nf} \Phi - \frac{\partial u_i}{\partial x_j} (\rho_{nf} \overline{u_i u_j}), \quad (38)$$

where Φ is the energy dissipation term,

$$\Phi = \left(\frac{\partial u_i}{\partial x_j} + \frac{\partial u_j}{\partial x_i} \right) \frac{\partial u_i}{\partial x_j}. \quad (39)$$

Clearly, the single-phase approach has advantages in ease of use, computational cost, while achieving good comparison with selected experimental data sets. However, the results depend strongly on the selected thermo-physical property models, especially for the thermal conductivity and viscosity. As mentioned, particle migration can significantly affect heat transfer results by creating non-uniform concentration fields, especially in entrance regions and boundary layers, particularly at large Peclet numbers, $Pe = Re \cdot Pr$.

Incorporating the slip between the particles and the fluids can improve the single-phase model by adding a virtual term in the thermal conductivity expression [118]. Furthermore, solving the NP-mass transfer equation together with the momentum and energy equations can also increase the accuracy [119].

2.3.2. Two-Phase Approach

Even if the ultra-fine particles can be uniformly suspended in the base fluid, several factors such as Brownian motion and thermophoresis can significantly affect the relative particle motion, leading to particle slip. Hence, two-phase models, which solve one set of governing equations for each of the phases, may be more suitable. The most used two-phase model for nanofluid flow and heat transfer is the so-called Eulerian–Eulerian model, where both phases are considered as “fluids” with volume fractions summing up to unity [120]. Specifically, the governing equations for phase α are as follows:

Continuity equation:

$$\frac{\partial(\varphi_{\alpha} \rho_{\alpha})}{\partial t} + \nabla(\varphi_{\alpha} \rho_{\alpha} u_{\alpha}) = 0; \quad (40)$$

Momentum equation:

$$\frac{\partial}{\partial t}(\varphi_{\alpha} \rho_{\alpha} u_{\alpha}) + \nabla(\varphi_{\alpha} \rho_{\alpha} u_{\alpha} u_{\alpha}) = -\varphi_{\alpha} \nabla p + \nabla \left[\varphi_{\alpha} \mu_{\alpha} \left(\nabla u_{\alpha} + (\nabla u_{\alpha})^T \right) \right] + F_{\alpha}; \quad (41)$$

Energy equation:

$$\frac{\partial (\varphi_\alpha \rho_\alpha h)}{\partial t} + \nabla [\varphi_\alpha \rho_\alpha u_\alpha h_\alpha] = \nabla (k_\alpha \nabla T_\alpha) + Q_\alpha. \tag{42}$$

F_α is the surface force due to the existence of another phase, and Q_α is the interface heat transfer term. Aside from the inclusion of volume fraction φ , the difference in Equations (40)–(42) from Equations (34)–(39) is due to interfacial momentum and energy change. The interfacial forces that may apply to nanofluid flow are discussed in the above sections. The rate of interface heat transfer between the nanoparticles (α) and the fluid (β) is

$$Q_{\alpha,\beta} = h_{\alpha,\beta} A_{\alpha,\beta} (T_\alpha - T_\beta), \tag{43}$$

where $A_{\alpha,\beta}$ is the interfacial area per unit volume.

Some studies employed the Eulerian-Lagrangian framework, which tracks the particle trajectories in the fluid phase. Still, a mixture model that introduces a term due to the drift of nanoparticles into the momentum equation of the base fluid is feasible [121]. However, the comparisons between different two-phase models suggest no obvious winner in terms of prediction accuracy. Hence, the Eulerian two-phase model is favored due to ease of use and low computational cost. It should be noted that, although the two-phase models are capable of capturing the non-uniform concentration fields, the turbulence intensity of the fluid phase were often assumed unaffected by the presence of the nanoparticle phase.

In some cases, it is more desirable to use a convection-diffusion equation to represent the dispersion process of NPs in the liquid medium. For example, the nanomedicine distribution in the systemic system can be described by

$$\frac{\partial c}{\partial t} + \nabla \cdot (\mathbf{v}c) = \nabla \cdot (D_{NP} \nabla c), \tag{44}$$

where c is the NP concentration, and D_{NP} is the NP diffusion coefficient. This Euler–Euler method, which assumes small NP loading, one-way fluid-particle coupling, and negligible NP coagulation, is often preferred over the Euler-Lagrange approach due to its minimized computational expense.

2.3.3. Nanofluid Transport in Porous Media

Fluid flow in porous medium is governed by the Darcy-Forchheimer law [122,123]:

$$\frac{\partial p}{\partial x_i} = -\frac{\mu}{K} u_j - \frac{C_f \rho |u_j| u_j}{\sqrt{K}}. \tag{45}$$

The Darcy-Forchheimer law states that the momentum loss of flow through a porous medium is the result of two effects, *i.e.*, the loss due to inertia and viscous effects. The first term on the right-hand side of the equation is the Darcy term due to the viscous effect, and the second term on the right-hand side is the Forchheimer term due to the inertia effect. Here, μ and ρ are the fluid viscosity and density, respectively, u_j is the superficial velocity vector, K is the permeability, and C_f is the inertia resistance factor. In the limit of negligible inertia effect ($Re < 10$, where $Re = u\sqrt{K}/\nu$), Equation (45) is reduced to Darcy’s law, *i.e.*, $\nabla p = -(\mu/K) \vec{v}$. The permeability α and the inertia coefficient C_f are both functions of the porosity of the medium, which is defined as the ratio of the total voids volume and the total volume of the porous media. For example, Ergun [124] provided

$$K = \frac{\varepsilon^3 \ell^2}{C(1 - \varepsilon)^2}, \tag{46}$$

where ℓ is the size of the pore, and $C = 150\text{--}180$.

The mathematical formulation of nanofluid flow in porous medium needs to incorporate the effect of the porosity and permeability. For example, assuming homogeneity and local thermal equilibrium in the porous medium, using Boussinesq approximation and Darcy’s law, the governing equations for two-phase nanofluid natural convection can be written as [122,125]

$$\frac{\partial}{\partial x_i}(\rho_{nf}u_i) = 0, \tag{47}$$

$$\frac{1}{\varepsilon} \frac{\partial(\rho_{nf}u_i)}{\partial t} = -\frac{\partial p}{\partial x_i} - \frac{\mu_{nf}}{K}u_i + \rho_{nf}g_i, \tag{48}$$

$$(\rho c_p)_m \frac{\partial T}{\partial t} + (\rho c_p)_{bf} u_i \frac{\partial T}{\partial x_i} = \frac{\partial}{\partial x_i} \left(k_m \frac{\partial T}{\partial x_i} \right) + \varepsilon (\rho c_p)_p D_{NP} \frac{\partial c}{\partial x_i} \frac{\partial T}{\partial x_i}, \text{ and} \tag{49}$$

$$\frac{\partial c}{\partial t} + \frac{1}{\varepsilon} u_i \frac{\partial c}{\partial x_i} = \frac{\partial}{\partial x_i} \left(D_{NP} \frac{\partial c}{\partial x_i} \right), \tag{50}$$

where the buoyancy term can be approximated by

$$\rho_{nf}g_i \cong \left[\varphi \rho_p + (1 - \varphi) \left\{ \rho_f (1 - \beta (T - T_0)) \right\} \right] g_i. \tag{51}$$

Here, the subscript m means the effective property of the porous medium. T is the nanofluid temperature, T_0 is a reference temperature, and β is the volume expansion coefficient. The superficial velocity u_i is used in the equations.

2.3.4. Magnetic Nanofluids

Magnetic nanofluids behave like a paramagnetic material. In the absence of a magnetic field, the magnetic moments of particles are randomly orientated due to Brownian motion, and the fluid has no net magnetization. When an external magnetic field is applied, the magnetic moments align along the magnetic field direction, generating net magnetization to the fluid. In the presence of a magnetic field, the governing equations of the fluid flow and heat transfer need to be modified to include the Lorentz force and the corresponding energy. The continuity equation remains unchanged, while the momentum equation becomes

$$\rho \frac{D\vec{v}}{Dt} = -\nabla p + \nabla \cdot \vec{\tau} + \rho \vec{g} + \vec{J} \times \vec{B}, \tag{52}$$

where \vec{v} is the velocity field, p is the pressure, D/Dt is the total derivative, \vec{g} is the gravitational acceleration, $\vec{\tau}$ is the deviatoric stress tensor, \vec{J} is the electric current density, and \vec{B} is the magnetic flux density. Owing to Ampere’s law, the Lorentz force term $\vec{J} \times \vec{B}$ can be written in the form

$$\vec{J} \times \vec{B} = \frac{(B \cdot \nabla) B}{\mu_0} - \nabla \left(\frac{B^2}{2\mu_0} \right). \tag{53}$$

The energy equation has the form

$$\left[\rho c_V - \mu_0 \vec{H} \cdot \left(\frac{\partial M}{\partial T} \right) \right] \left(\frac{\partial T}{\partial t} + \vec{v} \cdot \nabla T \right) + \mu_0 T \left(\frac{\partial M}{\partial T} \right) \cdot \frac{\partial \vec{H}}{\partial T} = k_{nf} \nabla^2 T + \mu_{nf} \Phi, \tag{54}$$

where $\mu_0 = 4\pi \times 10^{-7} \text{ H} \cdot \text{m}^{-1}$ is the magnetic constant, \vec{H} is the magnetic field intensity, M is the magnetization of the fluid, and $\mu_{nf} \Phi$ is the viscous dissipation term. As such, the fluid flow and heat transfer of magnetic nanofluids can be manipulated by applying different magnetic fields.

2.3.5. Nanofluid Transport in Thin Films

The behavior of a nanoparticle embedded in a moving film can be modeled using the Reynolds lubrication equation, which governs the pressure distribution of thin viscous fluid films [126]:

$$\frac{\partial}{\partial x} \left(\frac{\rho h^3}{12\mu} \frac{\partial p}{\partial x} \right) + \frac{\partial}{\partial y} \left(\frac{\rho h^3}{12\mu} \frac{\partial p}{\partial y} \right) = \frac{1}{2} \frac{\partial}{\partial x} [\rho h (u_a + u_b)] + \frac{1}{2} \frac{\partial}{\partial y} [\rho h (v_a + v_b)] + \rho (w_a - w_b) - \rho u_a \frac{\partial h}{\partial x} - \rho v_a \frac{\partial h}{\partial y} + h \frac{\partial \rho}{\partial t} \quad (55)$$

where p is the fluid-film pressure, x and y are the bearing width and length coordinates, and z is the vertical coordinate. In addition, h is the variable fluid-film thickness; u , v , and w are the film velocities in x -, y -, and z -direction, respectively; and subscripts a , b denote the top and bottom bounding wall-surfaces, respectively.

This equation can be derived from the Navier-Stokes equation, which assumes laminar incompressible flow of Newtonian fluids. In addition, the inertial force is neglected, pressure is assumed to be constant across the film, and there is no velocity-slip at the boundaries. For a journal bearing with variable fluid-film thickness (or spacing $h(\theta, z)$), the Reynolds equation can be simplified and normalized via [127]

$$\bar{h} = h/C, \theta = x/R, \bar{\mu} = \mu_{nf}/\mu_{bf}, \bar{z} = z/R, p = pC^2/\mu_{bf}\omega R^2. \quad (56)$$

Then, the modified non-dimensional Reynolds equation can be expressed as

$$\frac{\partial}{\partial \theta} \left(\frac{\bar{h}^3}{12\bar{\mu}} \frac{\partial \bar{p}}{\partial \theta} \right) + \frac{R^2}{L^2} \frac{\partial}{\partial \bar{z}} \left(\frac{\bar{h}^3}{12\bar{\mu}} \frac{\partial \bar{p}}{\partial \bar{z}} \right) = \frac{1}{2} \frac{\partial \bar{h}}{\partial \theta} \quad (57)$$

where the normalized film thickness can be modified to incorporate the effect of adjustment on the convectional film thickness:

$$\bar{h} = 1 + \varepsilon \cos(\theta') + R_{adj} + T_{adj}. \quad (58)$$

Here, C is the radial clearance, R is the radius of the journal, L is the length of the bearing, R_{adj} and T_{adj} are the normalized radial and tilt adjustment, and $\varepsilon = e/C$ is the normalized eccentricity.

3. Nanofluid Flow Applications

A major engineering goal in *thermal* nanofluid flow applications is to achieve high system performance, *i.e.*, optimal efficiency via a reduction in entropy increase. The methodology is briefly discussed in Section 3.1 with an application to nanofluid flow in a microchannel. Nanoparticles often appear in nature or as drugs in liquid form. Thus, under thermal conditions, droplet-size changes due to evaporation or condensation must be accounted for. Section 3.2 provides a modern application to multi-component droplet-vapor interactions.

Finally, in Sections 3.3 and 3.4 microsystem cooling with nanofluids and improved lubrication with metallic nanoparticles are reviewed, respectively.

3.1. Entropy Generation

Most studies considering thermal nanofluid flow have focused on the enhanced heat transfer. However, to optimize the thermal systems for the efficient removal of high heat fluxes, entropy generation minimization must be considered along with the heat transfer maximization. Entropy generation is the measure of process irreversibility caused by both heat transfer and friction effects. It can be employed to assess the performance of thermal devices. The local entropy-generation rate (S_{gen} in W/K) for convection heat transfer can be expressed as [103,128]

$$S_{gen} = S_{gen}(\text{thermal}) + S_{gen}(\text{friction}). \quad (59)$$

Clearly, Equation (59) encapsulates the irreversibility due to heat transfer and frictional effects, where

$$S_{gen}(\text{thermal}) = \frac{k}{T^2} \left[\left(\frac{\partial T}{\partial x} \right)^2 + \left(\frac{\partial T}{\partial y} \right)^2 + \left(\frac{\partial T}{\partial z} \right)^2 \right], \tag{60}$$

and

$$\begin{aligned} S_{gen}(\text{frictional}) &= \frac{\mu \Phi}{T} = \frac{\mu}{T} (\overline{\Phi} + \Phi') \\ &= \frac{\mu}{T} \left[\left(\frac{\partial \overline{u_i}}{\partial x_j} + \frac{\partial \overline{u_j}}{\partial x_i} \right) \frac{\partial \overline{u_i}}{\partial x_j} + \frac{\partial \overline{u_i}}{\partial x_j} \frac{\partial \overline{u_j}}{\partial x_i} \right]. \end{aligned} \tag{61}$$

The dissipation due to fluctuations in turbulent flow is roughly the same as that due to the mean flow [128]. In fact, the frictional entropy generation rate is only comparable to the thermal entropy generation rate when the flow Reynolds number is very large. It should be noted that, when using the above equations for nanofluids, the corresponding nanofluid properties should be used.

In the laminar regime of nanofluid flow, adding nanoparticles to the base fluid reduces entropy generation. An optimal NP concentration exists that corresponds to minimized entropy generation [15,129]. Moreover, the total entropy generation of the system can be reduced without significantly increasing the required pumping power [130]. Thus, adding nanoparticles to the base fluid can be very beneficial from a perspective of the second law of thermodynamics. In the turbulent flow regime, especially when the Reynolds number is very high, frictional entropy generation exceeds its thermal counterpart. In this case, adding NPs to the base fluid may push up the total entropy generation rate due to the augmented nanofluid viscosity [131]. Clearly, the thermo-physical properties of nanofluids play an important role in determining the entropy generation rate.

3.2. Nanodroplet-Vapor-Air Mixture Dynamics

A more specific set of governing equations are for the transport and phase change of inhaled nanodroplets in lung airways, which has rich roots in biomedical and engineering problems including administered drug-aerosols using inhalers, fume- or mist-nanodroplet inhalation from fuel handling, welding operation, spray processes, as well as smoke-aerosol inhalation from conventional cigarettes and electronic cigarettes. Their transport and conversion phenomena involve complex physical and thermodynamic interactions between air, vapors, and nanodroplets with their therapeutic (or toxic) compounds and the respiratory tract walls. This is an area of interdisciplinary applications of modern thermal internal nanofluid-flow engineering. A basic mathematical model can be outlined as follows, which is based on the work of Feng *et al.* [132].

Any given air-vapor mixture is described as a single continuous phase, *i.e.*, the conservation laws for mass, momentum, and energy describing the air-vapor mixture transport and the advection-diffusion equation describing vapor-species transport. Droplet-vapor interaction, *i.e.*, liquid-vapor mass change due to evaporation or condensation, is implemented by: (i) incorporating the energy generation/destruction due to phase change via source terms in the energy equation and vapor-species transport equations (see Equations (62)–(65)); and (ii) calculating the local vapor-mass fraction in the droplet mass conservation equation (see Equation (66)). Specifically, the energy equation of the air-vapor mixture reads

$$\begin{aligned} \frac{\partial(\rho c_p T)_{a-v}}{\partial t} + \frac{\partial(\rho c_p u_j T)_{a-v}}{\partial x_j} = \\ \frac{\partial}{\partial x_j} \left[\left(k_{a-v} + \frac{\rho_{a-v} c_{a-v,p} \nu_T}{Pr_T} \right) \frac{\partial T_{a-v}}{\partial x_j} \right] + \Phi + \frac{\partial}{\partial x_j} \left[\sum_{s=1}^N h_s \rho_{a-v} \left(\tilde{D}_{a-v} + \frac{\nu_T}{Sc_T} \right) \frac{\partial Y_s}{\partial x_j} \right] + S_{v-d}^{(E)}, \end{aligned} \tag{62}$$

where the energy source term $S_{v-d}^{(E)}$ is due to the latent heat of evaporation or condensation which is released or absorbed by the droplets per local mesh cell:

$$S_{v-d}^{(E)} = \sum_{s=1}^4 S_{v-d,s}^{(E)} = \left\{ \sum_{i=1}^{N_{d,cell}} \left[\left(\sum_{s=1}^4 L_s \bar{j}_s \right) A_d \right]_i \right\} / V_{cell}, \tag{63}$$

where $N_{d,cell}$ is the total droplet number in a specified mesh cell.

The governing equation for advection and diffusion of the sth vapor species is expressed as

$$\frac{\partial(\rho_{a-v} Y_{v,s})}{\partial t} + \frac{\partial}{\partial x_j} (\rho_{a-v} u_j Y_{v,s}) = \frac{\partial}{\partial x_j} \left[\rho_{a-v} \left(\tilde{D}_{a-v,s} + \frac{\nu_T}{Sc_T} \right) \frac{\partial Y_{v,s}}{\partial x_j} \right] + S_{v-d,s}^{(Y)}, \tag{64}$$

where $Sc_T = 0.9$ is the turbulence Schmidt number for $Y_{v,s}$, ν_T is the turbulent viscosity, and $\tilde{D}_{a-v,s}$ is the molecular diffusivity of the sth vapor species in the air-vapor mixture. The local vaporized/condensed vapor-mass flow rate of the aerosol components are added to its advection-diffusion equation as a source term $S_{v-d,s}^{(Y)}$ ($\text{kg} \cdot \text{m}^{-3} \cdot \text{s}^{-1}$), i.e.,

$$S_{v-d,s}^{(Y)} = \int_{t_{i,start}}^{t_{i,start} + \Delta t_f} \left(\sum_{i=1}^{N_{d,cell}} (\bar{j}_s A_d)_i \right) dt_d / (V_{cell} \Delta t_f), \tag{65}$$

where \bar{j}_s is the average evaporation/condensation mass flux normal to the droplet surface of the sth component (i.e., $\bar{j}_s > 0$ for evaporation and $\bar{j}_s < 0$ for condensation); and A_d is the droplet surface area. dt_d represents the droplet phase time differential, and Δt_f is the flow time-step.

For the multicomponent droplet size-change and transport, the governing equations for discrete droplets are the translational equation as well as the mass and energy conservation laws.

Newton’s second law of motion states

$$\frac{d}{dt} (m_d u_{d,i}) = F_i^D + F_i^L + F_i^{BM} + F_i^G, \tag{66}$$

where F_i^D , F_i^L , F_i^{BM} , and F_i^G are the drag force, lift force, Brownian motion-induced force, and gravity, respectively.

Droplet mass changes due to condensation/evaporation can be described as

$$\frac{dm_d}{dt} = - \sum_{s=1}^m \int_{surf} j_s dA \approx - \sum_{s=1}^m (\bar{j}_s \cdot A_d), \tag{67}$$

where the average mass flux \bar{j}_s is given by [133]:

$$\bar{j}_s = \rho_{a-v} \cdot C_m \cdot Sh \cdot \tilde{D}_{a-v,s} \cdot d_d^{-1} \ln \left[(1 - Y_{s,v,cell}) / (1 - Y_{s,v,surf}) \right]. \tag{68}$$

Here, Sh is the Sherwood number (see the Nomenclature for definition), while $Y_{s,v,surf}$ and $Y_{s,v,cell}$ are the mass fractions of the sth vapor phase at the droplet surface and at the center of the cell, where the droplet currently resides. The correction factor C_m for submicron droplets, considering non-continuum effects, can be expressed as

$$C_m = \frac{1 + Kn}{1 + \left(\frac{4}{3\alpha_m} + 0.377 \right) Kn + \frac{4}{3\alpha_m} Kn^2}, \tag{69}$$

where Kn is the Knudsen number, $Kn = 2\lambda_{a-v}/d_d$, in which λ_{a-v} is the mean free path of the air-vapor mixture surrounding the droplet; and α_m is the mass accommodation coefficient, where $\alpha_m = 1$ was

used in the present study [134]. The derivation of Equation (68) is based on the assumption that the distance between the droplet mass center and the mesh cell center is much larger than the droplet radius. Specifically, $Y_{s,v,cell}$ is determined by the advection-diffusion equation (see Equation (64)), while $Y_{s,v,surf}$ can be calculated by

$$Y_{s,v,surf} = \frac{\rho_{s,v,surf}}{\rho_{a-v}} = \frac{(P_{s,v,surf}/\Re_s T_d)}{\rho_{a-v}} = \frac{\gamma_s \cdot K_s \cdot X_{s,d} \cdot P_{s,v,sat}(T_d)}{\rho_{a-v} (\Re/M_s) T_d} \quad (70)$$

Here, $\rho_{s,v,surf}$ is the equivalent density of vapor species s in the air-vapor mixture at the droplet surface; γ_s is the activity coefficient of species s , which is a correction of the evaporation/condensation characteristics of a certain liquid component due to the molecular bonding changes in the pure droplets and in the multicomponent droplets [135]; $X_{s,d}$ is the mole fraction of the s th component in the droplet; \Re_s is the species gas constant; T_d is the droplet temperature; and $P_{s,v,sat}$ is the temperature-dependent saturation pressure of the pure s th species. Clearly, parameters γ_s and $X_{s,d}$ serve as corrections to the vapor pressure at the surface of multicomponent droplets (Raoult's law), while K_s is the correction factor for the Kelvin effect [134]:

$$K_s = \exp[4\sigma_s M_s / (\Re_s d_d T_d)], \quad (71)$$

where σ_s is the surface tension of component s at the droplet surface.

The droplet heat transfer equation takes on the form

$$m_d c_{p,d} \left(\frac{dT_d}{dt} \right) = C_T \left(k_{a-v} \cdot \frac{Nu}{d_d} \right) (T_{a-v,cell} - T_d) A_d - \left(\sum_{s=1}^N L_s \bar{j}_s \right) A_d, \quad (72)$$

where L_s is the latent heat of liquid-vapor phase transition of the s th species (L_s is always larger than zero). Moreover, C_T is the correction factor for submicron droplets:

$$C_T = \frac{1 + Kn}{1 + \left(\frac{4}{3\alpha_T} + 0.377 \right) Kn + \frac{4}{3\alpha_T} Kn^2}, \quad (73)$$

where α_T is the thermal accommodation coefficient with the value of $\alpha_T = 1$ [134].

The governing equations of the transport and phase change of the multicomponent droplet-vapor mixtures can be solved using computational fluid-particle dynamics (CF-PD) methods [103].

3.3. Nanofluids for Microsystem Cooling

Experimental studies have shown somewhat controversial results regarding the heat transfer performance of nanofluids in microsystems. Whether or not nanofluids outperform their base fluids is unclear. On the other hand, numerical studies tend to show that nanofluids have better heat transfer performance in microsystems as compared to their base fluids. This part reviews the numerical studies on microsystem cooling using nanofluids. As the numerical study of nanofluid flow and heat transfer in microsystems are abundant, only selective studies are reviewed here, which provide a good cover of the history and the state of the art.

By assuming that nanofluid has higher thermal conductivity and similar viscosity as base fluid, Lee and Choi [136] demonstrated that nanofluids offer a dramatic enhancement of cooling rates by reducing the thermal resistance of the microchannel heat sink significantly. Using a similar approach with empirical correlations of nanofluid properties, Chein and Huang [137] showed that the performance of a MCHS is greatly improved by using nanofluids in the laminar flow regime, without causing extra pressure loss. Koo and Kleinstreuer [138] conducted a numerical study of nanofluid flow in MCHS's using theoretical models of effective thermal conductivity and dynamic viscosity of nanofluids. They demonstrated that, at low volume fractions (<4%), nanofluid significantly increases

the heat transfer performance of microheat-sinks, given that particle accumulation is avoided. High aspect-ratio microchannel is recommended for better performance. Jang and Choi [139] numerically studied the effectiveness of using water-diamond nanofluid in a MCHS and found that, at a fixed pumping power, nanofluid with 1 vol % enhanced the cooling performance by 10% as compared to water. A theoretical model for nanofluid thermal conductivity was developed and used in this study, while the Einstein equation was adopted for nanofluid viscosity. Li and Kleinstreuer [140] studied heat transfer in a trapezoidal microchannel using a theoretical k_{nf} model, whose predictions agree well with available measured data in the literature. They suggested that nanofluids measurably enhance the thermal performance of microchannel mixture flow with a small penalty in pumping power. Lelea [141] and Lelea and Nisulescu [142] numerically investigated nanofluid flow in microchannels. They found that the enhancement of heat transfer due to the presence of NPs rises along the channels. The heat transfer enhancement for cooling and heating are different for the same NP concentration. Additionally, neglecting viscous heating effects would give incorrect predictions. Ting *et al.* [143] investigated the effects of streamwise conduction on the thermal performance of nanofluid flow in MCHS's under exponentially decaying wall heat flux. The Peclet number was found to strongly affect the temperature distribution when the streamwise conduction is incorporated. The effect of streamwise conduction became important when $Pe < 10$.

MCHS's can be treated as porous media so that, using an averaging approach, the heat transfer and friction characteristics can be obtained without considering each individual channels. Tasi and Chein [144] employed the two-equation averaging approach to study nanofluid cooled MCHS's, where the MCHS's were treated as a porous medium. They concluded that adding nanoparticles to the base fluid reduced the temperature difference between the heated wall and the fluid due to a reduction in the conductive thermal resistance. However, adding NPs increases the convective thermal resistance of the MCHS due to increased viscosity and decreased thermal capacity. Optimum values of channel aspect ratio and porosity exist, above which the thermal resistance of the MCHS is increased by adding NPs to the base fluid. Chen and Ding [145] employed the two-equation porous media approach to evaluate the thermal performance of a nanofluid-cooled MCHS. The model was tuned based on experimental measurements. Specifically, the effect of the inertia force term of the Forchheimer-Brinkman-extended Darcy equation on the thermal performance was assessed. Hatami and Ganji [146] treated MCHS's cooled by nanofluids as a porous medium and suggested high-channel aspect ratios, large NP size, and wide fins for better thermal performance.

Many studies have used the two-phase modeling approach to study nanofluid flow in microsystems. Kalteh *et al.* [147] used a Eulerian two-phase model to numerically study nanofluid laminar forced convection in a microchannel. The heat transfer enhancement was found to increase with the Re number and NP concentration, and with the decrease of the NP diameter. The model also predicted that the velocity and temperature difference between the fluid and the NP phase was negligible and that the NP concentration was uniform. Kalteh *et al.* [148] used experimental measurements to validate single-phase and two-phase nanofluid flow in MCHS's. The two-phase model showed better agreement with the measurements, though the velocity and temperature difference between the two phases was shown to be negligible. Fani *et al.* [149] used the two-phase model to study the size effect of the nanoparticle on the thermal performance of nanofluids in MCHS's. The increment of the NP size was shown to cause an increase in pressure drop and a decrease in heat transfer. Ghale *et al.* [150] evaluated single-phase and two-phase mixture models for the heat transfer of nanofluids in microchannels and concluded that the two-phase model achieved better agreement with experimental measurements. They also demonstrated that ribs at microchannels increased both the Nusselt number and the friction coefficient of nanofluids.

Alternative modeling methods have also been used to numerically study microsystem cooling using nanofluids. Sun *et al.* [115] reported an equilibrium molecular dynamics simulation of nanofluid thermal conductivity in a nanochannel. The thermal conductivity of the mixture was found to be anisotropic due to the confinement of the wall. Its value decreased with the increase of the channel

width owing to the wakened NP-wall interaction. Ahmed and Eslamian [151] used the multi-phase lattice Boltzmann method to evaluate the importance of particle-fluid slip on the laminar forced convection heat transfer in a microchannel. The results revealed the significance of Brownian force at $Re < 10$, where the nanofluid flow was heterogeneous and provided enhanced heat transfer as compared to the base fluid. At a higher Re number, the nanofluid flow was homogeneous, and no heat transfer augmentation was achieved. Thermophoresis effect was found to be insignificant at all Re number ranges. Karimipoura *et al.* [114] numerically studied nanofluid flow in a microchannel in slip flow regime using the lattice Boltzmann method. The results showed that decreasing the values of the slip coefficient enhances the convective heat transfer coefficient.

Entropy generation is a measure of the thermal performance of a system. It is an important factor to consider especially when designing a microsystem for enhanced heat transfer, where system efficiency is paramount [152]. Li and Kleinstreuer [129] conducted entropy generation analysis for nanofluid flow in trapezoidal microchannels with different aspect ratios. Optimal Reynolds number ranges were found to exist to operate the system based on minimization of total entropy generation. A suitable operational Reynolds-number range was found to be lower for microchannels with high aspect ratios. Ting *et al.* [153] analytically evaluated the effect of stream-wise conduction on the entropy generation of nanofluid flow in circular MCHS's under an exponentially decaying wall heat flux and constant pumping power conditions. The effect of stream-wise conduction was found to be important when the Peclet number was small, *i.e.*, irreversibility due to heat transfer dominants. Ting *et al.* [154] evaluated the entropy generation of viscous dissipative nanofluid flow in thermal non-equilibrium porous media embedded in microchannels. Results showed that, in a low-aspect-ratio microchannel, adding NPs to the base fluid decreased the thermodynamic efficiency, while using nanofluids in a high-aspect-ratio microchannel enhanced exergetic effectiveness in a low- Re flow regime. Cruz-Duarte *et al.* [155] demonstrated the design of a MCHS with nanofluids through the entropy generation minimization criterion.

In addition to microchannels and micro-heat sinks, alternative microsystems were considered for enhanced heat transfer using nanofluids [156]. For example, Mohammed *et al.* [157,158] numerically studied the thermal performance of microchannel heat exchangers using nanofluids for both parallel-flow and counter-flow scenarios. The results indicate that increasing NP loading and Reynolds number cause an increase in heat transfer performance of counter-flow heat exchangers, but deteriorations for parallel-flow scenarios. A slight increase in pressure drop was found due to the presence of NPs. An optimization study of microchannel heat exchangers was performed in [159]. Islami *et al.* [160,161] studied heat transfer and fluid flow in microchannels containing micromixers. Newtonian and non-Newtonian base fluids were considered. Heat transfer enhancement was shown to be more significant with Newtonian base fluids. Lelea and Laza [162] considered a micro-heat sink with straight microtubes and multiple tangential inlet jets. Employing a nanofluid showed little advantage as compared to the base fluid when a fixed pumping power was used.

Geometric optimization of nanofluid-cooled MCHS's has been conducted in a number of studies using different techniques [163–166]. For example, Mital [167] analyzed laminar, developing nanofluid flow in microchannels using empirical correlations. The results indicated that for an optimal volume fraction, heat transfer can be maximized at a given Re number.

Nanoparticle distribution in the flow field, especially near the wall, may have a significant effect on the fluid flow and heat transfer characteristics of nanofluids in microchannels. Alvariño *et al.* [168] assessed the self-diffusion of fully developed nanofluid flow in microchannels using a new CFD solver. They showed that, while thermophoresis may be negligible, self-diffusion can be significant. Furthermore, contrary to what has usually been assumed, self-diffusion, Brownian diffusion, and thermophoresis cannot be superimposed when determining a NP-concentration field. Hedayati *et al.* [169] investigated the effect of NP migration and asymmetric heating on the convection heat transfer of nanofluid flow in microchannels considering Brownian motion and thermophoretic diffusion. A particle depletion layer was detected near the wall, which contributed to an enhanced

heat transfer rate. This augmentation was found to be enhanced by a slip-boundary due to microscopic roughness. Nikkhaha *et al.* [170] numerically studied nanofluid flow in a microchannel with oscillating heat flux and slip boundary condition. Higher slip-coefficients and NP-volume fractions were found to increase the Nusselt number.

Convection heat transfer characteristics of nanofluids in microsystems in the presence of a magnetic field have also been the subject of a number of studies [171,172]. Malvandi and Ganji [173] and Malvandi *et al.* [174] found that a strong magnetic field had a negative effect on nanofluid performance. Hajialigol *et al.* [175] investigated nanofluid magneto-hydrodynamic mixed convection and entropy generation in a microchannel and revealed that the heat transfer increases with the Hartmann number. The total entropy generation was shown to decrease with increasing magnetic strength and volume fraction.

In conclusion, numerical studies indicate a better heat transfer performance of nanofluids in microsystems as compared to that of the base fluids; clearly, it is largely due to the models used for the effective thermal conductivities. Meanwhile, significant penalty in pressure drop were recorded by adding NPs to the base fluids.

3.4. Nanoparticles for Enhanced Lubrication

There are a very few numerical studies of enhanced lubrication using nanoparticles. This can be attributed to the fact that the lubrication process often involves the deformation of NPs, which is difficult to model. Nevertheless, some studies have revealed lubrication characteristics using numerical methods. This section reviews these studies on enhanced lubrication using nanoparticles.

The friction-related mechanisms of lubricants with nanoparticles can be deduced by analyzing scanning electron microscopy images and energy-dispersive spectrometry patterns of the wear surface. In addition, it can be probed by molecular level simulations. For example, Lv *et al.* [176] first used molecular dynamics (MD) simulation to study the friction mechanisms using nanofluid lubricants. They showed the rotations of NPs under low pressure as well as trapping and aggregations of NPs under higher pressures. These effects separated the friction surfaces and led to enhanced lubrication properties. The molecular dynamic simulation of Hu *et al.* [22] demonstrated that phase transition took place under high load, while the transition pressure of an NP-added lubricant was higher than that of the base lubricant. Nanoparticles could effectively increase the load-carrying capacity, especially for NPs with smaller sizes, due to stronger micro-motions and volume effects. Hu *et al.* [39] compared the differences in the mechanical properties of contact layers between friction surfaces with and without Cu-nanoparticles. The MD simulation results demonstrated better improvement in friction properties with Cu-nanoparticles at a low velocity compared with that at a high velocity. At low velocities, a Cu-nanofilm that was formed on the friction surface beard the velocity gradient and plastic deformation. Under high velocity conditions, a transfer layer that appeared adjacent to the interface reduced the friction forces. Hu *et al.* [177] numerically studied the tribological properties of two hard NPs confined by two iron blocks using an MD simulation. They showed that, at a low velocity and low load, the NPs separated the two blocks from each other and acted as ball bearings. At high velocity and high load, the support effect of these nanoparticles was lost in a short sliding time due to the crushing of the NPs. In another study using an MD simulation, Hu *et al.* [178] demonstrated that the improved load-carrying capacity is due to the organized molecular structures of the lubricant near the NPs, and to the deformation of nanoparticles.

Shenoy *et al.* [127] used a modified Reynolds equation to numerically investigate the effect of a nanoparticle additive on the fluid film of a journal bearing. The results indicated that dispersing TiO₂ nanoparticles in engine oil can reduce end-leakage as well as friction, thus improving the load capacity of the bearing featuring negative radial and tilt adjustments. Binu *et al.* [179] used the modified Krieger-Dougherty viscosity model to incorporate the nanoparticle effect on the fluid rheology. They introduced coupled stresses to the Reynolds equation to account for the impact of nanoparticles. The model predicted a significant increase in load-carrying capacity of the journal bearing by using a

TiO₂-based lubricant. Nicoletti [180] found that adding nanoparticles to the base oil modifies the volumetric heat capacity of the lubricant, resulting in lower temperature and thus higher viscosity for an improved load-carrying capacity.

Österle *et al.* [181] investigated the effect of the presence of soft and hard nanoparticles on the friction performance during dry sliding, employing the method of movable cellular automata. The results revealed that agglomerates of soft NPs decomposed and mixed with the oxide layer and reduced the friction coefficient, while that of hard NPs mixed with the oxide in the third body layer without decomposing. Increasing the amount of hard NPs would increase the friction coefficient. In another study, Österle *et al.* [182] numerically investigated the effect of the presence of SiC-NPs on the lubrication between tribofilms. They found that, though increasing the thickness of the tribofilm significantly reduced friction, the volume fraction of SiC-NPs only marginally affected the friction. Dmitriev *et al.* [183] showed that embedding silica-NPs in a polymer matrix tribofilm significantly affected the interface structure and smoothness of the sliding mechanism. Österle *et al.* [126] demonstrated that reduced friction and wear can be expected if the silica tribofilms are mixed with at least 10 vol % graphite.

4. Conclusions and Future Work

Adding nanoparticles to base liquids at low concentrations creates a complex mixture, where the small size of the particles and their large surface-to-volume ratio cause new physical phenomena that have not been observed in other suspensions. Hence, as part of the rich applications of nanofluids, the underlying physics of the nanoparticle-fluid suspension and their mathematical description need to be properly addressed. Nanoparticle aggregation poses a great challenge, due to the difficulties in characterizing the process and the potential deterioration of nanofluid performance. Clearly, more refined mathematical models are needed to accurately account for the aggregation process.

Nanofluids can provide superior cooling performance in microsystems for laminar intermediate-to-high Reynolds number flow conditions, without causing an excessive increase in pressure drop. However, possible nanoparticle deposition, *i.e.*, microchannel fouling, need to be properly addressed to ensure good performance of nanofluid flow and heat transfer. Numerical studies of nanofluid flow and heat transfer in microsystems are providing insight to improved system performance.

Using nanoparticles as additives to lubricants can greatly enhance their tribological properties by reducing friction and wear, as well as increase the load-carrying capacity. Low weight percentages of nanoparticles seem to provide the best performance. The mechanisms for enhanced lubrication performance are manifold and depend on the material structure of the nanoparticles. Under film-lubrication conditions, where the load is supported by the lubricant and any solid–solid contact is avoided, the potential increase of the lubricant's viscosity due to nanoparticle addition needs to be considered. Again, a homogeneous suspension of nanoparticles in lubricants is vital for proper applications, as large aggregates of nanoparticles may be detrimental to the lubrication process.

Acknowledgments: Zelin Xu acknowledges partial financial support via a CSC (Chinese Scholarship Council) award.

Author Contributions: Zelin Xu conducted the literature review and drafted and formatted the manuscript; Clement Kleinstreuer designed and revised the manuscript and finalized the submitted version.

Conflicts of Interest: The authors declare no conflict of interest.

Abbreviations

The following abbreviations are used in this manuscript:

MCHS	microchannel heat sink
MD	molecular dynamics
NP	nanoparticle

References

1. Kleinstreuer, C.; Xu, Z. Thermal nanofluid flow in microchannels with applications. In *Heat Transfer Enhancement with Nanofluids*; Bianco, V., Manca, O., Nardini, S., Vafai, K., Eds.; CRC Press: Boca Raton, FL, USA, 2015.
2. Kleinstreuer, C.; Xu, Z. Convection heat transfer in conduits with nanofluids. In *CRC Handbook of Thermal Engineering*, 2nd ed.; Chhabra, R.P., Ed.; CRC Press: Boca Raton, FL, USA, 2016.
3. Kleinstreuer, C. Computational nanofluid flow and heat transfer in microchannels. In *CRC Handbook of Fluid Dynamics*, 2nd ed.; Johnson, R.W., Ed.; CRC Press: Boca Raton, FL, USA, 2016; pp. 1–8.
4. Kleinstreuer, C.; Childress, E.M. Nanodrug delivery for tumor treatment. In *Encyclopedia of Microfluidics and Nanofluidics*; Li, D., Ed.; Springer: New York, NY, USA, 2015.
5. Kleinstreuer, C.; Childress, E.M.; Kennedy, A.S. Targeted drug delivery: Multifunctional nanoparticles and direct micro-drug delivery to tumors. In *Transport in Biological Media*; Becker, S.M., Kuznetsov, A.V., Eds.; Academic Press: Cambridge, MA, USA, 2013; pp. 391–416.
6. Kleinstreuer, C.; Feng, Y.; Childress, E.M. Drug-targeting methodologies with applications: A review. *World J. Clin. Cases* **2014**, *2*, 742–756. [[CrossRef](#)] [[PubMed](#)]
7. Xu, Z.; Jernigan, S.; Kleinstreuer, C.; Buckner, G.D. Solid tumor embolotherapy in hepatic arteries with an anti-reflux catheter system. *Ann. Biomed. Eng.* **2016**, *44*, 1036–1046. [[CrossRef](#)] [[PubMed](#)]
8. Fang, X.; Xuan, Y.; Li, Q. Experimental investigation on enhanced mass transfer in nanofluids. *Appl. Phys. Lett.* **2009**, *95*. [[CrossRef](#)]
9. Veilleux, J.; Coulombe, S. A dispersion model of enhanced mass diffusion in nanofluids. *Chem. Eng. Sci.* **2011**, *66*, 2377–2384. [[CrossRef](#)]
10. Kim, S.J.; Bang, I.C.; Buongiorno, J.; Hu, L.W. Surface wettability change during pool boiling of nanofluids and its effect on critical heat flux. *Int. J. Heat Mass Transf.* **2007**, *50*, 4105–4116. [[CrossRef](#)]
11. Kwark, S.M.; Kumar, R.; Moreno, G.; Yoo, J.; You, S.M. Pool boiling characteristics of low concentration nanofluids. *Int. J. Heat Mass Transf.* **2010**, *53*, 972–981. [[CrossRef](#)]
12. Michael, J.J.; Iniyar, S. Performance analysis of a copper sheet laminated photovoltaic thermal collector using copper oxide-water nanofluid. *Sol. Energy* **2015**, *119*, 439–451. [[CrossRef](#)]
13. Wu, Y.Y.; Wu, S.Y.; Xiao, L. Performance analysis of photovoltaic-thermoelectric hybrid system with and without glass cover. *Energy Convers. Manag.* **2015**, *93*, 151–159. [[CrossRef](#)]
14. Xu, Z.; Kleinstreuer, C. Concentration photovoltaic-thermal energy co-generation system using nanofluids for cooling and heating. *Energy Convers. Manag.* **2014**, *87*, 504–512. [[CrossRef](#)]
15. Xu, Z.; Kleinstreuer, C. Computational analysis of nanofluid cooling of high concentration photovoltaic cells. *J. Therm. Sci. Eng. Appl.* **2014**, *6*. [[CrossRef](#)]
16. Liu, G.L.; Kim, J.; Lu, Y.U.; Lee, L.P. Optofluidic control using photothermal nanoparticles. *Nat. Mater.* **2006**, *5*, 27–32. [[CrossRef](#)] [[PubMed](#)]
17. Taylor, R.A.; Phelan, P.E.; Otanicar, T.P.; Adrian, R.; Prasher, R. Nanofluid optical property characterization: Towards efficient direct absorption solar collectors. *Nanoscale Res. Lett.* **2011**, *6*, 1–11. [[CrossRef](#)] [[PubMed](#)]
18. Taylor, R.; Coulombe, S.; Otanicar, T.; Phelan, P.; Gunawan, A.; Lv, W.; Rosengarten, G.; Prasher, R.; Tyagi, H. Small particles, big impacts: A review of the diverse applications of nanofluids. *J. Appl. Phys.* **2013**, *113*. [[CrossRef](#)]
19. Ogihara, H.; Xie, J.; Okagaki, J.; Saji, T. Simple method for preparing superhydrophobic paper: Spray-deposited hydrophobic silica nanoparticle coatings exhibit high water-repellency and transparency. *Langmuir* **2012**, *28*, 4605–4608. [[CrossRef](#)] [[PubMed](#)]
20. Li, J.; Wu, R.; Jing, Z.; Yan, L.; Zha, F.; Lei, Z. One-step spray-coating process for the fabrication of colorful superhydrophobic coatings with excellent corrosion resistance. *Langmuir* **2015**, *31*, 10702–10707. [[CrossRef](#)] [[PubMed](#)]
21. Tao, X.; Jiazheng, Z.; Kang, X. The ball-bearing effect of diamond nanoparticles as an oil additive. *J. Phys. D Appl. Phys.* **1996**, *29*, 2932. [[CrossRef](#)]
22. Hu, C.; Bai, M.; Lv, J.; Wang, P.; Li, X. Molecular dynamics simulation on the friction properties of nanofluids confined by idealized surfaces. *Tribol. Int.* **2014**, *78*, 152–159. [[CrossRef](#)]
23. Spikes, H. Friction modifier additives. *Tribol. Lett.* **2015**, *60*, 1–26. [[CrossRef](#)]
24. Akbulut, M. Nanoparticle-based lubrication systems. *J. Powder Metall. Min.* **2012**, *1*. [[CrossRef](#)]

25. Choi, U.S. Enhancing thermal conductivity of fluids with nanoparticles. In Proceedings of the International Mechanical Engineering Congress and Exposition on Developments and Applications of Non-Newtonian Flows, San Francisco, CA, USA, 12–17 November 1995; Siginer, D.A., Wang, H.P., Eds.; ASME: New York, NY, USA FED-Vol. 231/MD-Vol. 66; pp. 99–105.
26. Kleinstreuer, C.; Li, J.; Koo, J. Microfluidics of nano-drug delivery. *Int. J. Heat Mass Transf.* **2008**, *51*, 5590–5597. [[CrossRef](#)]
27. Kandlikar, S.G. History, advances, and challenges in liquid flow and flow boiling heat transfer in microchannels: A critical review. *J. Heat Transf.* **2012**, *134*. [[CrossRef](#)]
28. Salman, B.H.; Mohammed, H.A.; Munisamy, K.M.; Kherbeet, A.S. Characteristics of heat transfer and fluid flow in microtube and microchannel using conventional fluids and nanofluids: A review. *Renew. Sustain. Energy Rev.* **2013**, *28*, 848–880. [[CrossRef](#)]
29. Chein, R.; Chuang, J. Experimental microchannel heat sink performance studies using nanofluids. *Int. J. Therm. Sci.* **2007**, *46*, 57–66. [[CrossRef](#)]
30. Jung, J.Y.; Oh, H.S.; Kwak, H.Y. Forced convective heat transfer of nanofluids in microchannels. *Int. J. Heat Mass Transf.* **2009**, *52*, 466–472. [[CrossRef](#)]
31. Ho, C.J.; Wei, L.C.; Li, Z.W. An experimental investigation of forced convective cooling performance of a microchannel heat sink with Al₂O₃/water nanofluid. *Appl. Therm. Eng.* **2010**, *30*, 96–103. [[CrossRef](#)]
32. Anoop, K.; Sadr, R.; Yu, J.; Kang, S.; Jeon, S.; Banerjee, D. Experimental study of forced convective heat transfer of nanofluids in a microchannel. *Int. Commun. Heat Mass Transf.* **2012**, *39*, 1325–1330. [[CrossRef](#)]
33. Byrne, M.D.; Hart, R.A.; da Silva, A.K. Experimental thermal–hydraulic evaluation of CuO nanofluids in microchannels at various concentrations with and without suspension enhancers. *Int. J. Heat Mass Transf.* **2012**, *55*, 2684–2691. [[CrossRef](#)]
34. Rimbault, B.; Nguyen, C.T.; Galanis, N. Experimental investigation of CuO-water nanofluid flow and heat transfer inside a microchannel heat sink. *Int. J. Therm. Sci.* **2014**, *84*, 275–292. [[CrossRef](#)]
35. Liu, D.; Yu, L. Single-phase thermal transport of nanofluids in a mini-channel. *J. Heat Transf.* **2011**, *133*. [[CrossRef](#)]
36. Manay, E.; Sahin, B. The effect of microchannel height on performance of nanofluids. *Int. J. Heat Mass Transf.* **2016**, *95*, 307–320. [[CrossRef](#)]
37. Azizi, Z.; Alamdari, A.; Malayeri, M.R. Thermal performance and friction factor of a cylindrical microchannel heat sink cooled by Cu-water nanofluid. *Appl. Therm. Eng.* **2016**, *99*, 970–978. [[CrossRef](#)]
38. Chevalier, J.; Tillement, O.; Ayela, F. Rheological properties of nanofluids flowing through microchannels. *Appl. Phys. Lett.* **2007**, *91*. [[CrossRef](#)]
39. Hu, C.; Bai, M.; Lv, J.; Liu, H.; Li, X. Molecular dynamics investigation of the effect of copper nanoparticle on the solid contact between friction surfaces. *Appl. Surf. Sci.* **2014**, *321*, 302–309. [[CrossRef](#)]
40. Zhang, Z.; Xue, Q.; Zhang, J. Synthesis, structure and lubricating properties of dialkyldithiophosphate-modified Mo-S compound nanoclusters. *Wear* **1997**, *209*, 8–12. [[CrossRef](#)]
41. Xue, Q.; Liu, W.; Zhang, Z. Friction and wear properties of a surface-modified TiO₂ nanoparticle as an additive in liquid paraffin. *Wear* **1997**, *213*, 29–32. [[CrossRef](#)]
42. Liu, W.; Chen, S. An investigation of the tribological behaviour of surface-modified ZnS nanoparticles in liquid paraffin. *Wear* **2000**, *238*, 120–124. [[CrossRef](#)]
43. Gao, Y.; Chen, G.; Oli, Y.; Zhang, Z.; Xue, Q. Study on tribological properties of oleic acid-modified TiO₂ nanoparticle in water. *Wear* **2002**, *252*, 454–458. [[CrossRef](#)]
44. Radice, S.; Mischler, S. Effect of electrochemical and mechanical parameters on the lubrication behaviour of Al₂O₃ nanoparticles in aqueous suspensions. *Wear* **2006**, *261*, 1032–1041. [[CrossRef](#)]
45. Battez, A.H.; González, R.; Viesca, J.L.; Fernández, J.E.; Fernández, J.D.; Machado, A.; Chou, R.; Riba, J. CuO, ZrO₂ and ZnO nanoparticles as antiwear additive in oil lubricants. *Wear* **2008**, *265*, 422–428. [[CrossRef](#)]
46. Tevet, O.; Von-Huth, P.; Popovitz-Biro, R.; Rosentsveig, R.; Wagner, H.D.; Tenne, R. Friction mechanism of individual multilayered nanoparticles. *Proc. Natl. Acad. Sci. USA* **2011**, *108*, 19901–19906. [[CrossRef](#)] [[PubMed](#)]
47. Tannous, J.; Dassenoy, F.; Lahouij, I.; le Mogne, T.; Vacher, B.; Bruhács, A.; Tremel, W. Understanding the tribochemical mechanisms of IF-MoS₂ nanoparticles under boundary lubrication. *Tribol. Lett.* **2011**, *41*, 55–64. [[CrossRef](#)]

48. Rapoport, L.; Moshkovich, A.; Perfilyev, V.; Laikhtman, A.; Lapsker, I.; Yadgarov, L.; Rosentsveig, R.; Tenne, R. High lubricity of re-doped fullerene-like MoS₂ nanoparticles. *Tribol. Lett.* **2012**, *45*, 257–264. [[CrossRef](#)]
49. Yadgarov, L.; Petrone, V.; Rosentsveig, R.; Feldman, Y.; Tenne, R.; Senatore, A. Tribological studies of rhenium doped fullerene-like MoS₂ nanoparticles in boundary, mixed and elasto-hydrodynamic lubrication conditions. *Wear* **2013**, *297*, 1103–1110. [[CrossRef](#)]
50. Shahnazar, S.; Bagheri, S.; Hamid, S.B.A. Enhancing lubricant properties by nanoparticle additives. *Int. J. Hydrog. Energy* **2016**, *41*, 3153–3170. [[CrossRef](#)]
51. Rapoport, L.; Leshchinsky, V.; Lapsker, I.; Volovik, Y.; Nepomnyashchy, O.; Lvovsky, M.; Popovitz-Biro, R.; Feldman, Y.; Tenne, R. Tribological properties of WS₂ nanoparticles under mixed lubrication. *Wear* **2003**, *255*, 785–793. [[CrossRef](#)]
52. Kalin, M.; Kogovšek, J.; Remškar, M. Mechanisms and improvements in the friction and wear behavior using MoS₂ nanotubes as potential oil additives. *Wear* **2012**, *280*, 36–45. [[CrossRef](#)]
53. Bartz, W.J. Some investigations on the influence of particle size on the lubricating effectiveness of molybdenum disulfide. *ASLE Trans.* **1972**, *15*, 207–215. [[CrossRef](#)]
54. Cusano, C.; Sliney, H.E. Dynamics of solid dispersions in oil during the lubrication of point contacts, Part I—Graphite. *ASLE Trans.* **1982**, *25*, 183–189. [[CrossRef](#)]
55. Cusano, C.; Sliney, H.E. Dynamics of solid dispersions in oil during the lubrication of point contacts, Part II—molybdenum disulfide. *ASLE Trans.* **1982**, *25*, 190–197. [[CrossRef](#)]
56. Zhou, J.; Yang, J.; Zhang, Z.; Liu, W.; Xue, Q. Study on the structure and tribological properties of surface-modified Cu nanoparticles. *Mater. Res. Bull.* **1999**, *34*, 1361–1367. [[CrossRef](#)]
57. Wang, Y.; Li, J.; Shan, L.; Chen, J.; Xue, Q. Tribological performances of the graphite like carbon films deposited with different target powers in ambient air and distilled water. *Tribol. Int.* **2014**, *73*, 17–24. [[CrossRef](#)]
58. Qiu, S.; Dong, J.; Cheng, G. A review of ultrafine particles as antiwear additives and friction modifiers in lubricating oils. *Lubr. Sci.* **1999**, *11*, 217–226.
59. Liu, G.; Li, X.; Qin, B.; Xing, D.; Guo, Y.; Fan, R. Investigation of the mending effect and mechanism of copper nano-particles on a tribologically stressed surface. *Tribol. Lett.* **2004**, *17*, 961–966. [[CrossRef](#)]
60. Mosleh, M.; Atnafu, N.D.; Belk, J.H.; Nobles, O.M. Modification of sheet metal forming fluids with dispersed nanoparticles for improved lubrication. *Wear* **2009**, *267*, 1220–1225. [[CrossRef](#)]
61. Hisakado, T.; Tsukizoe, T.; Yoshikawa, H. Lubrication mechanism of solid lubricants in oils. *J. Lubr. Technol.* **1983**, *105*, 245–252. [[CrossRef](#)]
62. Tenne, R. Inorganic nanotubes and fullerene-like nanoparticles. *Nat. Nanotechnol.* **2006**, *1*, 103–111. [[CrossRef](#)] [[PubMed](#)]
63. Wu, H.; Qin, L.; Zeng, Q.; Dong, G. Understanding the physical adsorption action mechanism of MoS₂ nanoparticles in boundary lubrication with different Polyisobutyleneamine Succinimide (PIBS) concentrations. *Tribol. Lett.* **2015**, *60*, 1–12. [[CrossRef](#)]
64. Liang, S.; Shen, Z.; Yi, M.; Liu, L.; Zhang, X.; Ma, S. In-situ exfoliated graphene for high-performance water-based lubricants. *Carbon* **2016**, *96*, 1181–1190. [[CrossRef](#)]
65. Xie, H.; Jiang, B.; He, J.; Xia, X.; Pan, F. Lubrication performance of MoS₂ and SiO₂ nanoparticles as lubricant additives in magnesium alloy-steel contacts. *Tribol. Int.* **2016**, *93*, 63–70. [[CrossRef](#)]
66. Rosentsveig, R.; Gorodnev, A.; Feuerstein, N.; Friedman, H.; Zak, A.; Fleischer, N.; Tannous, J.; Dassenoy, F.; Tenne, R. Fullerene-like MoS₂ nanoparticles and their tribological behavior. *Tribol. Lett.* **2009**, *36*, 175–182. [[CrossRef](#)]
67. Paskvale, S.; Remškar, M.; Čekada, M. Tribological performance of TiN, TiAlN and CrN hard coatings lubricated by MoS₂ nanotubes in Polyalphaolefin oil. *Wear* **2016**, *352*, 72–78. [[CrossRef](#)]
68. Luo, J.; Wen, S.; Huang, P. Thin film lubrication. Part I. Study on the transition between EHL and thin film lubrication using a relative optical interference intensity technique. *Wear* **1996**, *194*, 107–115. [[CrossRef](#)]
69. Shen, M.; Luo, J.; Wen, S. The tribological properties of oils added with diamond nano-particles. *Tribol. Trans.* **2001**, *44*, 494–498. [[CrossRef](#)]
70. Peng, D.X.; Kang, Y.; Hwang, R.M.; Shyr, S.S.; Chang, Y.P. Tribological properties of diamond and SiO₂ nanoparticles added in paraffin. *Tribol. Int.* **2009**, *42*, 911–917. [[CrossRef](#)]

71. Zhang, Y.; Li, C.; Jia, D.; Zhang, D.; Zhang, X. Experimental evaluation of the lubrication performance of MoS₂/CNT nanofluid for minimal quantity lubrication in Ni-based alloy grinding. *Int. J. Mach. Tools Manuf.* **2015**, *99*, 19–33. [[CrossRef](#)]
72. Zhang, Y.; Li, C.; Jia, D.; Li, B.; Wang, Y.; Yang, M.; Hou, Y.; Zhang, X. Experimental study on the effect of nanoparticle concentration on the lubricating property of nanofluids for MQL grinding of Ni-based alloy. *J. Mater. Process. Technol.* **2016**, *232*, 100–115. [[CrossRef](#)]
73. Jia, D.; Li, C.; Zhang, Y.; Zhang, D.; Zhang, X. Experimental research on the influence of the jet parameters of minimum quantity lubrication on the lubricating property of Ni-based alloy grinding. *Int. J. Adv. Manuf. Technol.* **2016**, *82*, 617–630. [[CrossRef](#)]
74. Nam, J.S.; Kim, D.H.; Chung, H.; Lee, S.W. Optimization of environmentally benign micro-drilling process with nanofluid minimum quantity lubrication using response surface methodology and genetic algorithm. *J. Clean. Prod.* **2015**, *102*, 428–436. [[CrossRef](#)]
75. Yu, X.; Jiang, Z.; Zhao, J.; Wei, D.; Zhou, C.; Huang, Q. Effects of grain boundaries in oxide scale on tribological properties of nanoparticles lubrication. *Wear* **2015**, *332*, 1286–1292. [[CrossRef](#)]
76. Yu, X.; Jiang, Z.; Zhao, J.; Wei, D.; Zhou, J.; Zhou, C.; Huang, Q. The role of oxide-scale microtexture on tribological behaviour in the nanoparticle lubrication of hot rolling. *Tribol. Int.* **2016**, *93*, 190–201. [[CrossRef](#)]
77. Zareh-Desari, B.; Abaszadeh-Yakhforvazani, M.; Khalilpourazary, S. The effect of nanoparticle additives on lubrication performance in deep drawing process: Evaluation of forming load, friction coefficient and surface quality. *Int. J. Precis. Eng. Manuf.* **2015**, *16*, 929–936. [[CrossRef](#)]
78. Wang, L.; Gao, Y.; Li, Z.; Zhou, A.; Li, P. Preparation and tribological properties of surface-modified ZnS nanoparticles. *Lubr. Sci.* **2015**, *27*, 241–250. [[CrossRef](#)]
79. Alves, S.M.; Mello, V.S.; Faria, E.A.; Camargo, A.P.P. Nanolubricants developed from tiny CuO nanoparticles. *Tribol. Int.* **2016**, in press. [[CrossRef](#)]
80. Sui, T.; Song, B.; Wen, Y.H.; Zhang, F. Bifunctional hairy silica nanoparticles as high-performance additives for lubricant. *Sci. Rep.* **2016**, *6*. [[CrossRef](#)] [[PubMed](#)]
81. Yang, C.; Hou, X.; Li, Z.; Li, X.; Yu, L.; Zhang, Z. Preparation of surface-modified lanthanum fluoride-graphene oxide nanohybrids and evaluation of their tribological properties as lubricant additive in liquid paraffin. *Appl. Surf. Sci.* **2015**, in press. [[CrossRef](#)]
82. Verma, A.; Jiang, W.; Abu Safe, H.H.; Brown, W.D.; Malshe, A.P. Tribological behavior of deagglomerated active inorganic nanoparticles for advanced lubrication. *Tribol. Trans.* **2008**, *51*, 673–678. [[CrossRef](#)]
83. Battez, A.H.; Viesca, J.L.; González, R.; Blanco, D.; Asedegbega, E.; Osorio, A. Friction reduction properties of a CuO nanolubricant used as lubricant for a NiCrBSi coating. *Wear* **2010**, *268*, 325–328. [[CrossRef](#)]
84. Jiao, D.; Zheng, S.; Wang, Y.; Guan, R.; Cao, B. The tribology properties of alumina/silica composite nanoparticles as lubricant additives. *Appl. Surf. Sci.* **2011**, *257*, 5720–5725. [[CrossRef](#)]
85. Zhang, B.S.; Xu, B.S.; Xu, Y.; Gao, F.; Shi, P.J.; Wu, Y.X. Cu nanoparticles effect on the tribological properties of hydrosilicate powders as lubricant additive for steel-steel contacts. *Tribol. Int.* **2011**, *44*, 878–886. [[CrossRef](#)]
86. Lahouij, I.; Vacher, B.; Martin, J.M.; Dassenoy, F. IF-MoS₂ based lubricants: Influence of size, shape and crystal structure. *Wear* **2012**, *296*, 558–567. [[CrossRef](#)]
87. Luo, T.; Wei, X.; Zhao, H.; Cai, G.; Zheng, X. Tribology properties of Al₂O₃/TiO₂ nanocomposites as lubricant additives. *Ceram. Int.* **2014**, *40*, 10103–10109. [[CrossRef](#)]
88. Rabaso, P.; Ville, F.; Dassenoy, F.; Diaby, M.; Afanasiev, P.; Cavoret, J.; Vacher, B.; le Mogne, T. Boundary lubrication: Influence of the size and structure of inorganic fullerene-like MoS₂ nanoparticles on friction and wear reduction. *Wear* **2014**, *320*, 161–178. [[CrossRef](#)]
89. Bogunovic, L.; Zuenkeler, S.; Toensing, K.; Anselmetti, D. An oil-based lubrication system based on nanoparticulate TiO₂ with superior friction and wear properties. *Tribol. Lett.* **2015**, *59*, 1–12. [[CrossRef](#)]
90. Ghaednia, H.; Hossain, M.S.; Jackson, R.L. Tribological performance of silver nanoparticle-enhanced polyethylene glycol lubricants. *Tribol. Trans.* **2015**. [[CrossRef](#)]
91. Xu, Z. An Improved Thermal Conductivity Model for Nanofluids with Applications to Concentration Photovoltaic-Thermal Systems. Master's Thesis, North Carolina State University, Raleigh, NC, USA, 2014.
92. Michaelides, E.E. Transport properties of nanofluids. A critical review. *J. Non-Equilib. Thermodyn.* **2013**, *38*, 1–79. [[CrossRef](#)]
93. McNab, G.S.; Meisen, A. Thermophoresis in liquids. *J. Colloid Interface Sci.* **1973**, *44*, 339–346. [[CrossRef](#)]
94. Hunter, R.J. *Foundations of Colloid Science*; Oxford University Press: New York, NY, USA, 2001.

95. Shukla, R.K.; Dhir, V.K. Effect of Brownian motion on thermal conductivity of nanofluids. *J. Heat Transf.* **2008**, *130*. [[CrossRef](#)]
96. Kleinstreuer, C.; Feng, Y. Thermal nanofluid property model with application to nanofluid flow in a parallel-disk System—Part I: A new thermal conductivity model for nanofluid flow. *J. Heat Transf.* **2012**, *134*. [[CrossRef](#)]
97. Buongiorno, J. Convective transport in nanofluids. *J. Heat Transf.* **2006**, *128*, 240–250. [[CrossRef](#)]
98. Ghadimi, A.; Saidur, R.; Metselaar, H.S.C. A review of nanofluid stability properties and characterization in stationary conditions. *Int. J. Heat Mass Transf.* **2011**, *54*, 4051–4068. [[CrossRef](#)]
99. Saidur, R.; Leong, K.Y.; Mohammad, H.A. A review on applications and challenges of nanofluids. *Renew. Sustain. Energy Rev.* **2011**, *15*, 1646–1668. [[CrossRef](#)]
100. Nan, C.W.; Birringer, R.; Clarke, D.R.; Gleiter, H. Effective thermal conductivity of particulate composites with interfacial thermal resistance. *J. Appl. Phys.* **1997**, *81*, 6692–6699. [[CrossRef](#)]
101. Maxwell, J.C. *A Treatise on Electricity and Magnetism*; Clarendon Press: Oxford, UK, 1881.
102. Yu, W.; Choi, S.U.S. The role of interfacial layers in the enhanced thermal conductivity of nanofluids: A renovated Maxwell model. *J. Nanopart. Res.* **2003**, *5*, 167–171. [[CrossRef](#)]
103. Kleinstreuer, C. *Microfluidic and Nanofluidics: Theory and Selected Applications*; John Wiley: Hoboken, NJ, USA, 2014.
104. Mahbulbul, I.M.; Saidur, R.; Amalina, M.A. Latest developments on the viscosity of nanofluids. *Int. J. Heat Mass Transf.* **2012**, *55*, 874–885. [[CrossRef](#)]
105. Prasher, R.; Song, D.; Wang, J.; Phelan, P. Measurements of nanofluid viscosity and its implications for thermal applications. *App. Phys. Lett.* **2006**, *89*. [[CrossRef](#)]
106. Timofeeva, E.V.; Routbort, J.L.; Singh, D. Particle shape effect on thermophysical properties of alumina nanofluids. *J. Appl. Phys.* **2009**, *106*. [[CrossRef](#)]
107. Halelfadl, S.; Maré, T.; Estellé, P. Efficiency of carbon nanotubes water based nanofluids as coolants. *Exp. Therm. Fluid Sci.* **2014**, *53*, 104–110. [[CrossRef](#)]
108. Einstein, A. Eine neue bestimmung der moleküldimensionen. *Ann. Phys.* **1906**, *324*, 289–306. [[CrossRef](#)]
109. Brinkman, H.C. The viscosity of concentrated suspensions and solutions. *J. Chem. Phys.* **1952**, *20*, 571–571. [[CrossRef](#)]
110. Corcione, M. Empirical correlating equations for predicting the effective thermal conductivity and dynamic viscosity of nanofluids. *Energy Convers. Manag.* **2011**, *52*, 789–793. [[CrossRef](#)]
111. Sarkar, J. A critical review on convective heat transfer correlations of nanofluids. *Renew. Sustain. Energy Rev.* **2011**, *15*, 3271–3277. [[CrossRef](#)]
112. Sundar, L.S.; Singh, M.K. Convective heat transfer and friction factor correlations of nanofluid in a tube and with inserts: A review. *Renew. Sustain. Energy Rev.* **2013**, *20*, 23–35. [[CrossRef](#)]
113. Yu, W.; France, D.M.; Timofeeva, E.V.; Singh, D.; Routbort, J.L. Comparative review of turbulent heat transfer of nanofluids. *Int. J. Heat Mass Transf.* **2012**, *55*, 5380–5396. [[CrossRef](#)]
114. Karimipour, A.; Nezhad, A.H.; D’Orazio, A.; Esfe, M.H.; Safaei, M.R.; Shirani, E. Simulation of copper-water nanofluid in a microchannel in slip flow regime using the lattice Boltzmann method. *Eur. J. Mech. B Fluids* **2015**, *49*, 89–99. [[CrossRef](#)]
115. Sun, C.; Lu, W.Q.; Liu, J.; Bai, B. Molecular dynamics simulation of nanofluid’s effective thermal conductivity in high-shear-rate Couette flow. *Int. J. Heat Mass Transf.* **2011**, *54*, 2560–2567. [[CrossRef](#)]
116. Yang, J.C.; Li, F.C.; Cai, W.H.; Zhang, H.N.; Yu, B. On the mechanism of convective heat transfer enhancement in a turbulent flow of nanofluid investigated by DNS and analyses of POD and FSP. *Int. J. Heat Mass Transf.* **2014**, *78*, 277–288. [[CrossRef](#)]
117. Abu-Nada, E. Dissipative particle dynamics simulation of natural convection using variable thermal properties. *Int. Commun. Heat Mass Transf.* **2015**, *69*, 84–93. [[CrossRef](#)]
118. Mokmeli, A.; Saffar-Avval, M. Prediction of nanofluid convective heat transfer using the dispersion model. *Int. J. Therm. Sci.* **2010**, *49*, 471–478. [[CrossRef](#)]
119. Kamyar, A.; Saidur, R.; Hasanuzzaman, M. Application of computational fluid dynamics (CFD) for nanofluids. *Int. J. Heat Mass Transf.* **2012**, *55*, 4104–4115. [[CrossRef](#)]
120. Bahiraei, M.; Hosseinalipour, S.M. Thermal dispersion model compared with Euler-Lagrange approach in simulation of convective heat transfer for nanoparticle suspensions. *J. Dispers. Sci. Technol.* **2013**, *34*, 1778–1789. [[CrossRef](#)]

121. Behroyan, I.; Vanaki, S.M.; Ganesan, P.; Saidur, R. A comprehensive comparison of various CFD models for convective heat transfer of Al₂O₃ nanofluid inside a heated tube. *Int. Commun. Heat Mass Transf.* **2016**, *70*, 27–37. [[CrossRef](#)]
122. Nield, D.A.; Kuznetsov, A.V. Thermal instability in a porous medium layer saturated by a nanofluid. *Int. J. Heat Mass Transf.* **2009**, *52*, 5796–5801. [[CrossRef](#)]
123. Mahdi, R.A.; Mohammed, H.A.; Munisamy, K.M.; Saeid, N.H. Review of convection heat transfer and fluid flow in porous media with nanofluid. *Renew. Sustain. Energy Rev.* **2015**, *41*, 715–734. [[CrossRef](#)]
124. Ergun, S. Fluid flow through packed columns. *Chem. Eng. Prog.* **1952**, *48*, 89–94.
125. Tzou, D.Y. Thermal instability of nanofluids in natural convection. *Int. J. Heat Mass Transf.* **2008**, *51*, 2967–2979. [[CrossRef](#)]
126. Hamrock, B.J.; Schmid, S.R.; Jacobson, B.O. *Fundamentals of Fluid Film Lubrication*, 2nd ed.; CRC Press: Boca Raton, FL, USA, 2004.
127. Shenoy, B.S.; Binu, K.G.; Pai, R.; Rao, D.S.; Pai, R.S. Effect of nanoparticles additives on the performance of an externally adjustable fluid film bearing. *Tribol. Lett.* **2012**, *45*, 38–42. [[CrossRef](#)]
128. Bejan, A. *Entropy Generation Minimization: The Method of Thermodynamic Optimization of Finite-Size Systems and Finite-Time Processes*; CRC Press: Boca Raton, FL, USA, 1996.
129. Li, J.; Kleinstreuer, C. Entropy generation analysis for nanofluid flow in microchannels. *J. Heat Transf.* **2010**, *132*. [[CrossRef](#)]
130. Feng, Y.; Kleinstreuer, C. Nanofluid convective heat transfer in a parallel-disk system. *Int. J. Heat Mass Transf.* **2010**, *53*, 4619–4628. [[CrossRef](#)]
131. Mahian, O.; Kianifar, A.; Kleinstreuer, C.; Al-Nimr, M.A.; Pop, I.; Sahin, A.Z.; Wongwises, S. A review of entropy generation in nanofluid flow. *Int. J. Heat Mass Transf.* **2013**, *65*, 514–532.
132. Feng, Y.; Kleinstreuer, C.; Castro, N.; Rostami, A. Computational transport, phase change and deposition analysis of inhaled multicomponent droplet-vapor mixtures in an idealized human upper lung model. *J. Aerosol Sci.* **2016**, *96*, 96–123. [[CrossRef](#)]
133. Turns, S.R. *An Introduction to Combustion*; McGraw-Hill: New York, NY, USA, 1996; Volume 287.
134. Hinds, W.C. *Aerosol Technology: Properties, Behavior, and Measurement of Airborne Particles*, 2nd ed.; John Wiley & Sons: New York, NY, USA, 1999.
135. Tu, H.H.; Ray, A.K. Measurement of activity coefficients from unsteady state evaporation and growth of microdroplets. *Chem. Eng. Commun.* **2005**, *192*, 474–498. [[CrossRef](#)]
136. Lee, S.; Choi, S.U.S. *Application of Metallic Nanoparticle Suspensions in Advanced Cooling Systems*; No. ANL/ET/CP-90558; CONF-961105-20; Argonne National Lab.: Argonne, IL, USA, 1996.
137. Chein, R.; Huang, G. Analysis of microchannel heat sink performance using nanofluids. *Appl. Therm. Eng.* **2005**, *25*, 3104–3114. [[CrossRef](#)]
138. Koo, J.; Kleinstreuer, C. Laminar nanofluid flow in microheat-sinks. *Int. J. Heat Mass Transf.* **2005**, *48*, 2652–2661. [[CrossRef](#)]
139. Jang, S.P.; Choi, S.U. Cooling performance of a microchannel heat sink with nanofluids. *Appl. Therm. Eng.* **2006**, *26*, 2457–2463. [[CrossRef](#)]
140. Li, J.; Kleinstreuer, C. Thermal performance of nanofluid flow in microchannels. *Int. J. Heat Fluid Flow* **2008**, *29*, 1221–1232. [[CrossRef](#)]
141. Lelea, D. The performance evaluation of Al₂O₃/water nanofluid flow and heat transfer in microchannel heat sink. *Int. J. Heat Mass Transf.* **2011**, *54*, 3891–3899. [[CrossRef](#)]
142. Lelea, D.; Nisulescu, C. The micro-tube heat transfer and fluid flow of water based Al₂O₃ nanofluid with viscous dissipation. *Int. Commun. Heat Mass Transf.* **2011**, *38*, 704–710. [[CrossRef](#)]
143. Ting, T.W.; Hung, Y.M.; Guo, N. Entropy generation of nanofluid flow with streamwise conduction in microchannels. *Energy* **2014**, *64*, 979–990. [[CrossRef](#)]
144. Tsai, T.H.; Chein, R. Performance analysis of nanofluid-cooled microchannel heat sinks. *Int. J. Heat Fluid Flow* **2007**, *28*, 1013–1026. [[CrossRef](#)]
145. Chen, C.H.; Ding, C.Y. Study on the thermal behavior and cooling performance of a nanofluid-cooled microchannel heat sink. *Int. J. Therm. Sci.* **2011**, *50*, 378–384. [[CrossRef](#)]
146. Hatami, M.; Ganji, D.D. Thermal and flow analysis of microchannel heat sink (MCHS) cooled by Cu-water nanofluid using porous media approach and least square method. *Energy Convers. Manag.* **2014**, *78*, 347–358. [[CrossRef](#)]

147. Kalteh, M.; Abbassi, A.; Saffar-Avval, M.; Harting, J. Eulerian–Eulerian two-phase numerical simulation of nanofluid laminar forced convection in a microchannel. *Int. J. Heat Fluid Flow* **2011**, *32*, 107–116. [[CrossRef](#)]
148. Kalteh, M.; Abbassi, A.; Saffar-Avval, M.; Frijns, A.; Darhuber, A.; Harting, J. Experimental and numerical investigation of nanofluid forced convection inside a wide microchannel heat sink. *Appl. Therm. Eng.* **2012**, *36*, 260–268. [[CrossRef](#)]
149. Fani, B.; Abbassi, A.; Kalteh, M. Effect of nanoparticles size on thermal performance of nanofluid in a trapezoidal microchannel-heat-sink. *Int. Commun. Heat Mass Transf.* **2013**, *45*, 155–161. [[CrossRef](#)]
150. Ghale, Z.Y.; Haghshenasfard, M.; Esfahany, M.N. Investigation of nanofluids heat transfer in a ribbed microchannel heat sink using single-phase and multiphase CFD models. *Int. Commun. Heat Mass Transf.* **2015**, *68*, 122–129. [[CrossRef](#)]
151. Ahmed, M.; Eslamian, M. Laminar forced convection of a nanofluid in a microchannel: Effect of flow inertia and external forces on heat transfer and fluid flow characteristics. *Appl. Therm. Eng.* **2015**, *78*, 326–338. [[CrossRef](#)]
152. Shalchi-Tabrizi, A.; Seyf, H.R. Analysis of entropy generation and convective heat transfer of Al₂O₃ nanofluid flow in a tangential micro heat sink. *Int. J. Heat Mass Transf.* **2012**, *55*, 4366–4375. [[CrossRef](#)]
153. Ting, T.W.; Hung, Y.M.; Guo, N. Effects of streamwise conduction on thermal performance of nanofluid flow in microchannel heat sinks. *Energy Convers. Manag.* **2014**, *78*, 14–23. [[CrossRef](#)]
154. Ting, T.W.; Hung, Y.M.; Guo, N. Entropy generation of viscous dissipative nanofluid flow in thermal non-equilibrium porous media embedded in microchannels. *Int. J. Heat Mass Transf.* **2015**, *81*, 862–877. [[CrossRef](#)]
155. Cruz-Duarte, J.M.; Garcia-Perez, A.; Amaya-Contreras, I.M.; Correa-Cely, C.R. Designing a microchannel heat sink with colloidal coolants through the entropy generation minimisation criterion and global optimisation algorithms. *Appl. Therm. Eng.* **2016**, *100*, 1052–1062. [[CrossRef](#)]
156. Sabaghan, A.; Edalatpour, M.; Moghadam, M.C.; Roohi, E.; Niazmand, H. Nanofluid flow and heat transfer in a microchannel with longitudinal vortex generators: Two-phase numerical simulation. *Appl. Therm. Eng.* **2016**, *100*, 179–189. [[CrossRef](#)]
157. Mohammed, H.A.; Bhaskaran, G.; Shuaib, N.H.; Abu-Mulaweh, H.I. Influence of nanofluids on parallel flow square microchannel heat exchanger performance. *Int. Commun. Heat Mass Transf.* **2011**, *38*, 1–9. [[CrossRef](#)]
158. Mohammed, H.A.; Bhaskaran, G.; Shuaib, N.H.; Saidur, R. Numerical study of heat transfer enhancement of counter nanofluids flow in rectangular microchannel heat exchanger. *Superlattices Microstruct.* **2011**, *50*, 215–233. [[CrossRef](#)]
159. Mohammadian, S.K.; Seyf, H.R.; Zhang, Y. Performance augmentation and optimization of aluminum oxide-water nanofluid flow in a two-fluid microchannel heat exchanger. *J. Heat Transf.* **2014**, *136*. [[CrossRef](#)]
160. Islami, S.B.; Dastvareh, B.; Gharraei, R. Numerical study of hydrodynamic and heat transfer of nanofluid flow in microchannels containing micromixer. *Int. Commun. Heat Mass Transf.* **2013**, *43*, 146–154. [[CrossRef](#)]
161. Islami, S.B.; Dastvareh, B.; Gharraei, R. An investigation on the hydrodynamic and heat transfer of nanofluid flow, with non-Newtonian base fluid, in micromixers. *Int. J. Heat Mass Transf.* **2014**, *78*, 917–929. [[CrossRef](#)]
162. Lelea, D.; Laza, I. The water based Al₂O₃ nanofluid flow and heat transfer in tangential microtube heat sink with multiple inlets. *Int. J. Heat Mass Transf.* **2014**, *69*, 264–275. [[CrossRef](#)]
163. Wang, X.D.; An, B.; Lin, L.; Lee, D.J. Inverse geometric optimization for geometry of nanofluid-cooled microchannel heat sink. *Appl. Therm. Eng.* **2013**, *55*, 87–94. [[CrossRef](#)]
164. Wang, X.D.; An, B.; Xu, J.L. Optimal geometric structure for nanofluid-cooled microchannel heat sink under various constraint conditions. *Energy Convers. Manag.* **2013**, *65*, 528–538. [[CrossRef](#)]
165. Halelfadl, S.; Adham, A.M.; Mohd-Ghazali, N.; Maré, T.; Estellé, P.; Ahmad, R. Optimization of thermal performances and pressure drop of rectangular microchannel heat sink using aqueous carbon nanotubes based nanofluid. *Appl. Therm. Eng.* **2014**, *62*, 492–499. [[CrossRef](#)]
166. Yang, Y.T.; Tang, H.W.; Ding, W.P. Optimization design of micro-channel heat sink using nanofluid by numerical simulation coupled with genetic algorithm. *Int. Commun. Heat Mass Transf.* **2016**, *72*, 29–38. [[CrossRef](#)]
167. Mital, M. Analytical analysis of heat transfer and pumping power of laminar nanofluid developing flow in microchannels. *Appl. Therm. Eng.* **2013**, *50*, 429–436. [[CrossRef](#)]
168. Alvariano, P.F.; Jabardo, J.S.; Agras, J.P.; del Valle, J.G. Self-diffusion assessment in laminar developed flow of nanofluids in microchannels. *Int. J. Therm. Sci.* **2015**, *98*, 113–123. [[CrossRef](#)]

169. Hedayati, F.; Domairry, G. Nanoparticle migration effects on fully developed forced convection of TiO₂-water nanofluid in a parallel plate microchannel. *Particuology* **2016**, *24*, 96–107. [[CrossRef](#)]
170. Nikkhah, Z.; Karimipour, A.; Safaei, M.R.; Forghani-Tehrani, P.; Goodarzi, M.; Dahari, M.; Wongwises, S. Forced convective heat transfer of water/functionalized multi-walled carbon nanotube nanofluids in a microchannel with oscillating heat flux and slip boundary condition. *Int. Commun. Heat Mass Transf.* **2015**, *68*, 69–77. [[CrossRef](#)]
171. Zhao, G.; Jian, Y.; Li, F. Streaming potential and heat transfer of nanofluids in microchannels in the presence of magnetic field. *J. Magn. Magn. Mater.* **2016**, *407*, 75–82. [[CrossRef](#)]
172. Bahiraei, M.; Hangi, M. Flow and heat transfer characteristics of magnetic nanofluids: A review. *J. Magn. Magn. Mater.* **2015**, *374*, 125–138. [[CrossRef](#)]
173. Malvandi, A.; Ganji, D.D. Effects of nanoparticle migration and asymmetric heating on magnetohydrodynamic forced convection of alumina/water nanofluid in microchannels. *Eur. J. Mech. B Fluids* **2015**, *52*, 169–184. [[CrossRef](#)]
174. Malvandi, A.; Kaffash, M.H.; Ganji, D.D. Nanoparticles migration effects on magnetohydrodynamic (MHD) laminar mixed convection of alumina/water nanofluid inside microchannels. *J. Taiwan Inst. Chem. Eng.* **2015**, *52*, 40–56. [[CrossRef](#)]
175. Hajjaligol, N.; Fattahi, A.; Ahmadi, M.H.; Qomi, M.E.; Kakoli, E. MHD mixed convection and entropy generation in a 3-D microchannel using Al₂O₃-water nanofluid. *J. Taiwan Inst. Chem. Eng.* **2015**, *46*, 30–42. [[CrossRef](#)]
176. Lv, J.; Bai, M.; Cui, W.; Li, X. The molecular dynamic simulation on impact and friction characters of nanofluids with many nanoparticles system. *Nanoscale Res. Lett.* **2011**, *6*. [[CrossRef](#)] [[PubMed](#)]
177. Hu, C.; Bai, M.; Lv, J.; Kou, Z.; Li, X. Molecular dynamics simulation on the tribology properties of two hard nanoparticles (diamond and silicon dioxide) confined by two iron blocks. *Tribol. Int.* **2015**, *90*, 297–305. [[CrossRef](#)]
178. Hu, C.; Bai, M.; Lv, J.; Li, X. Molecular dynamics simulation of mechanism of nanoparticle in improving load-carrying capacity of lubricant film. *Comput. Mater. Sci.* **2015**, *109*, 97–103. [[CrossRef](#)]
179. Binu, K.G.; Shenoy, B.S.; Rao, D.S.; Pai, R. Static characteristics of a fluid film bearing with TiO₂ based nanolubricant using the modified Krieger-Dougherty viscosity model and couple stress model. *Tribol. Lett.* **2014**, *75*, 69–79. [[CrossRef](#)]
180. Nicoletti, R. The importance of the heat capacity of lubricants with nanoparticles in the static behavior of journal bearings. *J. Tribol.* **2014**, *136*, 044502. [[CrossRef](#)]
181. Österle, W.; Dmitriev, A.I.; Kloß, H. Possible impacts of third body nanostructure on friction performance during dry sliding determined by computer simulation based on the method of movable cellular automata. *Tribol. Int.* **2012**, *48*, 128–136. [[CrossRef](#)]
182. Österle, W.; Dmitriev, A.I.; Kloß, H. Assessment of sliding friction of a nanostructured solid lubricant film by numerical simulation with the method of movable cellular automata (MCA). *Tribol. Lett.* **2014**, *54*, 257–262. [[CrossRef](#)]
183. Dmitriev, A.I.; Österle, W.; Wetzel, B.; Zhang, G. Mesoscale modeling of the mechanical and tribological behavior of a polymer matrix composite based on epoxy and 6 vol % silica nanoparticles. *Comput. Mater. Sci.* **2015**, *110*, 204–214. [[CrossRef](#)]

